Delft University of Technology

Bachelor Final Project Thesis

Double BSc program Applied Physics and Applied Mathematics

Conductance of a nanowire with nonlinear electrostatics

Author:
Piotr Benedysiuk

Supervisors:
Dr. M.B. van Gijzen
Dr. A.R. Akhmerov

Other committee members:
Dr. M Wimmer
Msc. A. Vuik
Dr. J.L.A. Dubbeldam
Dr. J.G. Spandaw

Abstract

The electrostatics has effect on conductance of nanowire devices. In this model electrostatics are described by nonlinear coupling of the Poisson and the Schrödinger equations. In presence of magnetic and electric field and spin-orbit interaction, conductance develops a feature called the helical gap. This gap is characterised by a drop of conductance and is the main focus of the research.

The solver is based around an Anderson mixing scheme, and specific class of points has been discovered for which the solver performs poorly. For those points, an temperature annealing subroutine has been put in place to speed up convergence. This subroutine efficiently solves the system for some small finite temperature. The solver has also been expanded to solve systems for magnetic field pointed in any direction of the y, z plane.

As a result, it is now possible to perform simulations for different magnitudes and directions of magnetic field, which are a handy tool for understanding the behaviour of conductance as a function of V_G in real nanowires. The relation between energy and conductance has been researched. The size of helical gap is found to scale linearly with the Zeeman energy E_Z, while other features of conductance scale nonlinearly.

Contents

Chapter 1

Introduction

The field of quantum technologies has been gathering lots of wind in it's sails. New, smaller devices are being researched and the media hypes over the wonders of quantum computers. Serious businesses and organisations start to invest heavily in the quantum devices, like Google and Intel. Recent announcement about the Quantum Flagship initiative by the EU shows that political organisations start to follow the trend as well. In this exciting era of inventions a corner stone of nano devices has been researched in, among many places, TU Delft. This corner stone is the nanowire device.

Nanowires are structures whose cross sections are bounded to sizes in order of tens of nanometers. The length of such structures isn't bounded to any significant limitation, and they are far longer than wide in practice. When cooled down to temperatures in the range of mili Kelvins naive models expect the conductance of such system to change in quantized steps directly relating to energy dispersion relations of the system. Actual devices, due to impurities, finite temperatures and interfaces between different parts of device, exhibit conductance similar to quantized steps with some added smooth transitions between the steps. This means that the naive models are essentially valid, and predictions made from them are of use to describe the physics of nanowire devices. One can observe unique features if one tunes the strength of magnetic and electric field right in such a device. The feature we mostly focus on is the behaviour of conductance for different electric fields. For fixed external magnetic field, one can change the external electric field. This result in conductance of the wire to have a $0 \rightarrow 2 \rightarrow 1 \rightarrow 2$ shape as a function of electric field. The area corresponding to conductance of one is called the helical gap.

Theoretically this is a well understood phenomenon, yet many models describe such systems in terms of tunable energy of an electron trapped in a 2D cross section of a nanowire. In practice this parameter isn't directly tunable. Instead, one can change the potential of local electric field called gate voltage V_G. To relate V_G to energy correctly, one must consider the electrostatic potential generated by the electrons present in the system. The electrostatics can change simple energy relations derived from more naive models into nonlinear scaling relations. Inclusion of electrostatics involves solving a non linearly coupled Schrödinger - Poisson (SP) equation.

This SP equation is solved numerically by use of an algorithm based on Anderson Mixing scheme, developed as master project [2]. This solver can solve the system of equations for various magnitudes of magnetic field and strengths of spin orbit interactions.

The helical gap is closely related to the magnetic field. The energy dispersion of electrons in the system has an energy gap between the spin up and spin down branch caused by the Zeeman effect. When the Fermi level lies inside of this gap, the conductance of the wire is lower than outside of it and more specifically, only mostly spin down electrons conduct (as opposed to mostly spin up electrons). The direction of the applied magnetic field has a tremendous effect, to the extend that for a magnetic field aligned perpendicularly to the wire the helical gap ceases to be. For this reason, the numerical solver must be expanded to be able to perform calculations for various directions of magnetic field.

Another development needed, is a way to be able to do simulations for very fine ranges of V_G. Some specific points, which are the focal point of the phenomena of conductance, prove to give rise to numerical problems for the solver.

This structure of this thesis is as follows: chapter 2 describes a InSb nanowire device, geometrically at first and then through description of quantum effects working on electrons in such a wire. The main computational issue is introduced - a non linear coupling of SP equation, due to the electrostatic effect caused by electrons present in the system. A relation between energy and momenta k, called energy dispersion, is derived and from there one introduces the notion of conductance. Effect of strength the parameters on the shape of energy dispersion and effect of the shape of energy dispersion on the shape of the conductance are introduced. Chapter closes by introducing numerical values of relevant constants and energy scales.
Chapter 3 begins by stating the SP problem in terms of discretizated meshes and explain the approach to solve it. Few numerical algorithms are introduced, especially the Anderson method used to vastly improve the convergence speed. Attempts of memory and relaxation parameters optimization together with convergence analysis of Anderson are next. The analysis leads to discovery of specific points for which the Anderson performs the worst. Lastly a temperature annealing subroutine is introduced in order to improve convergence in those points and is showed to work for specific temperature ranges.
Chapter 4 starts by showing energies corresponding to a range of V_G. Then, full picture of conductance is introduced in terms of fixed magnetic field magnitude E_Z but changing direction θ and tunable energy. Scaling properties of few conductance plateaus are researched in terms of E_Z and V_G. After, the full conductance is introduced in terms of V_G and θ. Afterwards, more focus is put on the E_Z as the scaling properties between conductance in terms of tunable energy and E_Z are compared to conductance in terms of V_G and E_Z.
The thesis closes with a conclusion, with acknowledgements right after.

Chapter 2

Quantum effects in InSb nanowires

In this chapter one introduces general InSb device see section 2.1. Afterwards section 2.2 introduces the effect magnetic and electric field have on the device, with section 2.3 stating a interaction in the system that's very hard to calculate - electrostatics. Section 2.4 put all that interactions together to state the full Hamiltonian working on the system, and from there derives the energy dispersion relation. Influence parameters have on the dispersion is shown together the influence they have on conductance. Chapter finishes with a introduction of all numerical values used to describe the system and energy scales.

2.1 Description of the system

Nanowire devices are simplified to three building blocks for this project. First, the nanowire is a hexagonal shaped Indium Antimonide (InSb) semiconductor. It has about 100 nm of diameter in the x, y section and is considered to be infinite in the z direction see figure 2.1 on the left.

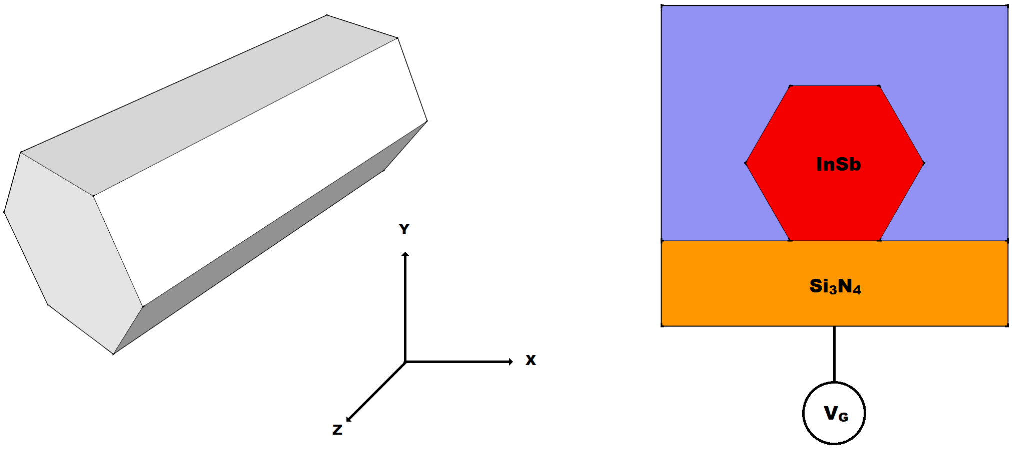

Figure 2.1: On the left, a sketch of nanowire, with added coordinates. Wire is bounded in x and y direction and infinite in the z direction. On the right, schematic picture of a global backgate device. Circle denoted by V_G stands for the voltage source that can be tuned in real experiments.

On top of the nanowire lies a piece of dielectric material Silicon Nitride (Si3N4). Its whole purpose in actual devices is to separate the nanowire from the third and final element. This element is a (global) voltage gate, used to create an electric field inside of the nanowire without allowing electrons to flow into the system. One does that by applying a finite potential difference V_G at the boundary of the dielectric. Silicon Nitride is perfect for this purpose, due to the fact that it's an insulator and it thus doesn't allow electrons to flow through. This device is sketched in figure 2.1 on the right.

The whole device is z-direction invariant. Consider a part of the wire with length Δz as a unit cell. The function describing the electrons inside of this unit cell must be Δz periodic. Yet, since the wire is exactly the same at all z, this function must be constant in the z-direction. Thus, once can choose any length of Δz and still have a viable unit cell. In this case, a natural choice is to choose the cross section in x, y direction with the infinitesimal width dz as a unit cell. One can invoke the Bloch theorem to describe conductance electrons (and thus electrons moving in the z direction) [1]. This ensures the form of conduction electrons to be:

$$\Psi_{i,k}(x,y,z) = \begin{bmatrix}\uparrow \\ \downarrow\end{bmatrix} U_{i,k}(x,y)e^{ikz} \tag{2.1}$$

where subscripts i, k correspond to orbitals in the cross section and momentum along the wire respectively. The $\begin{bmatrix}\uparrow \\ \downarrow\end{bmatrix}$ describes the spin state of said electron and is a 2×1 complex vector, $U_{i,k}$ is the wavefunction in the cross section.

2.2 Zeeman induced gap and spin orbit interactions

Electrons are mass carrying particles. One associates kinetic energy $\frac{\hat{p}\cdot\hat{p}}{2m^*}$ with such particles. Here $\hat{p}$ is the momentum of an electron and m^* is the effective mass of a particle. This effective mass is a material property, changing mass of electron corresponding to crystal structure of the material. The momenta operator reads $\hat{p} = -i\hbar\nabla$, with $\hbar$ the Planck constant, thus we can introduce the first energy operator entering the Hamiltonian as:

$$H_{kinetic} = -\frac{\hbar^2}{2m^*}\nabla^2\sigma_0, \tag{2.2}$$

where σ_0 is a 2×2 identity matrix making $H_{kinetic}$ a diagonal operator. Electrons, being spin $\frac{1}{2}$ particles, experience different forces based on their spin direction. When an external magnetic field $\mathcal{B}$ is applied, the (energy) degenerate orbitals of an electron (higher eigenmodes of the electron) split due to the so called Zeeman Effect. The associated Zeeman energy E_Z enters the Hamiltonian of the system in the form of the operator

$$H_{Zeeman} = \gamma\hat{\sigma}\cdot\mathcal{B}, \tag{2.3}$$

where $\gamma = 9.27\cdot 10^{-24}$ J/T is called the Bohr magneton, $\hat{\sigma}$ is a vector of Pauli matrices. The Pauli matrices read:

$$\sigma_x = \begin{bmatrix} 0 & 1 \\ 1 & 0 \end{bmatrix}, \tag{2.4}$$

$$\sigma_y = \begin{bmatrix} 0 & -i \\ i & 0 \end{bmatrix}, \tag{2.5}$$

$$\sigma_z = \begin{bmatrix} 1 & 0 \\ 0 & -1 \end{bmatrix}, \tag{2.6}$$

Since the external magnetic field is a global property of the device, it is not place dependent and we can express the eigenenergy (eigenvalue) of this operator as $E_Z\hat{\sigma}\cdot\hat{r}$, where $\hat{r}$ is the direction of magnetic field and $E_Z = \gamma\cdot|\mathcal{B}|$. The magnetic field can point in any direction in the z, y space so we can state the final operator as

$$H_{Zeeman} = E_Z(\cos(\theta)\sigma_z + \sin(\theta)\sigma_y), \tag{2.7}$$

where θ is the tilt in magnetic field taking orientation along z as a zero.

For example, consider a system containing two free electrons of the same momenta but opposite spin orientations. The energy of the electrons in the same system with applied magnetic field in the direction of spin will differ by exactly $2E_Z$. The Zeeman effect has been measured in a number of systems, like Hydrogen atoms.

Another effect related to spin of a particle is the spin orbit (SO) interaction. Consider an electron moving with momentum $\hat{p}$ through an electric field. In electron rest-frame the electric field is moving and thus induces an magnetic field $B_{induced} \propto E\times\hat{p}$. This induced magnetic field gives a rise to a momentum dependent Zeeman effect called spin orbit coupling. SO coupling linear in momenta is known as Rashba SO and enters the Hamiltonian as

$$H_{Rashba} = \frac{\alpha}{\hbar}(\hat{r}_{induced}\times\hat{p})\cdot\hat{\sigma}, \tag{2.8}$$

where, $\hat{r}_{induced}$ is the direction of the electric field and α is know as the SO strength. In practice a different parameter called SO length l_{SO} is used to describe the magnitude of the SO effect.

Consider an electron with spin orientation not perpendicular to the electric field. As stated before the moving (in electrons frame of reference) electric field induces a magnetic field. This magnetic field exerts Lorentz force $F = \frac{e}{m^*}\hat{p} \times B_{induced}$ on an electron, where e is the electron charge, aligning the spin with the induced field. Thus the direction of spin moves around, an effect called spin-flip. l_{SO} is a typical length scale on which such flip happens.

The Rashba operator interacts with any electric field present in the system. This can make the equations, and in turn calculations, very cumbersome so one restricts the SO to only interact with a virtual potential difference applied along the wire. This potential difference corresponds to the electric field one needs to apply in real world situations in order to get electric current and the strength of it can be varied by changing the strength of SO strength. One considers this potential to be virtual because it doesn't enter the calculations expect for giving rise to a SO operator used:

$$H_{SO} = \frac{\alpha}{\hbar} p_z \sigma_y = -i\alpha \frac{\partial}{\partial z} \sigma_y. \tag{2.9}$$

H_{SO} is an off diagonal operator. SO coupling has been observed and used in many quantum mechanical systems and gave rise to the specialised field of spin-orbitronics [4].

2.3 Electric potential due to electrons in the nanowire

The core of the problem arises when one considers the electrostatic potential term. Electrons experience Coulomb force from other electrons, and thus the amount and position of the electrons in the system determine the electrostatic potential ϕ.

Charge density in this model is described by a fully the quantum-mechanical approach. Every electron present in the system contributes one charge quantum to the density, with the chance the charge is present at some x, y given by $|U_{i,k}(x, y)|^2$. One assumes here that the $U_{i,k}$ from equation (2.1) are orthogonal with respect to each other for different values of i. One then account for all electrons in the system by integrating over all the energies and summing over all the possible eigenmodes of the wire's cross section.

$$\rho(x, y) = \sum_i \int_{-\infty}^{\infty} f(E, E_F, T)|U_{i,k}(x, y)|^2 D_i(E) dE \tag{2.10}$$

with density of states (DoS) $D_i(E) = \frac{1}{2\pi}\frac{dk}{dE(k)}$ describing how many states occupy an energy, and $f(E, E_F, T)$ the Fermi-Dirac distribution describing influence temperature has on the distribution of states across the energy spectrum

$$f(E, E_F, T) = \left(\exp\left(\frac{E - E_F}{k_B T}\right) + 1\right)^{-1}, \tag{2.11}$$

the Fermi energy E_F is a reference energy and k_B the Boltzmann constant. For energies larger than E_F the Fermi-Dirac decreases exponentially, ensuring that equation (2.10) is finite. The subscript i stands for different eigenenergies of the cross sectional area of the wire. In the limit case $T \rightarrow 0$ the Fermi-Dirac distribution approaches a step function, so when one disregards temperature effects the charge density becomes:

$$\rho(x,y) = \sum_i \int\limits_{E \leq E_F} |U_{i,k}(x,y)|^2 D_i(E) dE, \tag{2.12}$$

Equation (2.12) clearly describes the physical meaning of the Fermi level E_F. All the electron states with energy above E_F don't contribute to charge density. Since, by definition, electrons carry charge and thus contribute to charge density, electron states above E_F aren't occupied by electrons for a system at $T = 0$. Instead those states are left vacant. One can relate the charge density with the electric potential using the familiar Poisson equation to get:

$$\nabla^2 \phi(x,y) = -\frac{\rho(x,y)}{\epsilon(x,y)}, \tag{2.13}$$

where $\epsilon(x,y)$ stands for the dielectric constant of the medium. Inspection of figure 2.1 shows that the whole system consists essentialy of two area's, each one with a constant ϵ. As stated before, electrons experience Coulomb force so electrostatic potential operator enters the Hamiltonian as diagonal operator:

$$H_{electrostatics} = -e\phi(x,y)\sigma_0 \tag{2.14}$$

2.4 Energy dispersion and conductance

The previous sections describe various interactions an electron can experience within the framework of this model. Since all those Hamiltonian operators commute with each other, $[H_i, H_j] = 0 \; \forall i,j$, one can state the total Hamiltonian of the system as a simple sum of those Hamiltonian operators:

$$\mathcal{H} = -\big(\frac{\hbar^2}{2m^*}\nabla^2 + e\phi(x,y)\big)\sigma_0 - i\alpha\frac{\partial}{\partial z}\sigma_y + E_Z(\cos(\theta)\sigma_z + \sin(\theta)\sigma_y) \tag{2.15}$$

Common practice is expressing the energy and Hamiltonian in units of $\frac{\hbar^2}{2m^*}$ to simplify the equations. Using the fact that all operators work either purely on cross section or direction along the wire one writes:

$$\mathcal{H} = H_z + H_{x,y} \tag{2.16}$$

$$H_z = -\frac{\partial^2}{\partial z^2}\sigma_0 + \alpha\frac{\partial}{\partial z}\sigma_y + E_Z(\cos(\theta)\sigma_z + \sin(\theta)\sigma_y) \tag{2.17}$$

$$H_{x,y} = -(\frac{\partial^2}{\partial x^2} + \frac{\partial^2}{\partial y^2} + e\phi(x,y))\sigma_0 \tag{2.18}$$

From here one can derive a relation, referred to as the energy dispersion, between eigenenergies of this Hamiltonian and momentum k, see Appendix A.

$$E(k) = k^2 + E_i \pm \sqrt{(\alpha k + E_z\sin(\theta))^2 + (E_z\cos(\theta))^2)} \tag{2.19}$$

The ± sign creates two branches of the energy dispersion referred to as the lower and upper branch. Equation 2.12 integrates over all eigenenergies lower than E_F in order to determine potential ϕ. Yet, the potential term determines the eigenenergies of cross section E_i. This leaves us with a nonlinear coupled set of equations:

$$\begin{cases} \mathcal{H}(\phi)\Psi_{i,k}(x,y,z) = E\Psi_{i,k}(x,y,z) \\ \nabla^2\phi(x,y) = -\frac{\rho(x,y)}{\epsilon(x,y)} \end{cases} \tag{2.20}$$

Figure 2.2 explores the effect of parameters on the overall shape of energy dispersion. Three different types dispersion are shown: in the leftmost figure we have $\alpha = 0$ and E_Z is varied. One can see the energy gap widen between the ± parts of dispersion, for zero E_Z one has a degenerate parabola with the bottom at E_i. The middle plot is the situation of $E_Z = 0$, has a shape of letter V stacked on top of W. For stronger α the depth of the minimums of W increases. The upper band of dispersion gets steeper as α increases. An intuitive way of thinking of this is the following: the Zeeman effect pushes the local maxima of bands away from each other, while SO pushes local minimum of the W away from the local maximum. This implies some relation between E_Z and α must hold for the dispersion to be W shaped. One can derive (see Appendix A) that the dispersion has 2 local minimums (and thus W shape) if $\alpha^2 > 4E_Z$ for all θ. For specific case of $\theta = 0$ it is sufficient to have $\alpha^2 > 2E_Z$ in order for dispersion to have a W shape. This research focuses mostly on W shaped dispersions. Figure on the right is an example for such W shaped dispersion. If one changes the direction of magnetic field θ, the dispersion will 'tilt'. Both bands of dispersion tilt towards each other and at $\theta = \pm\pi/2$ the Zeeman gap closes.

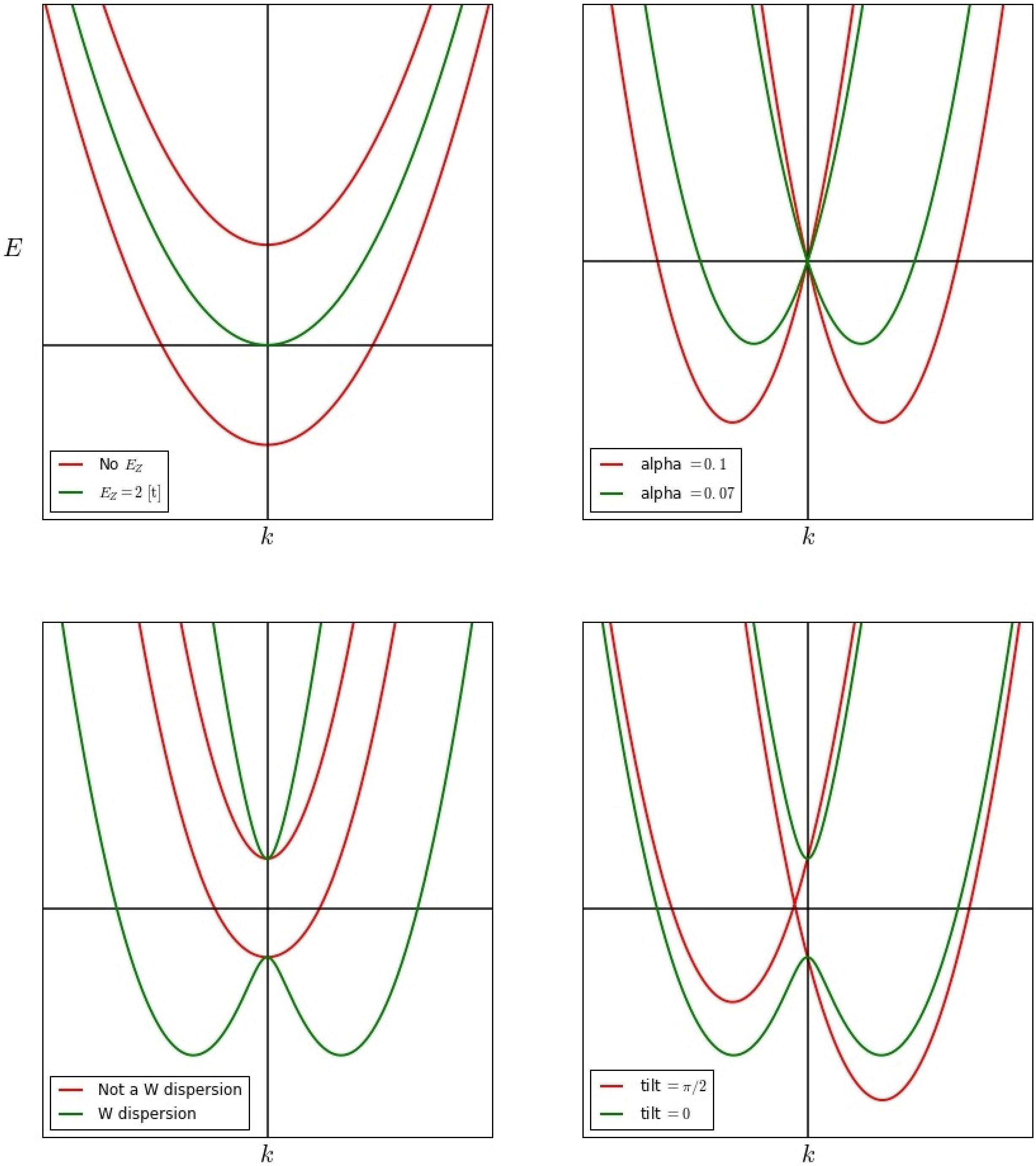

Figure 2.2: Schematic energy dispersion and effect of (left to right, top to bottom): Zeeman splitting, SO coupling, relation between E_Z and α for $\theta = 0$ and lastly relation between W dispersions and θ. All parameters that are not mentioned are set to zero. In third plot one considers case $\alpha^2 > 2E_Z$ and $\alpha^2 < 2E_Z$ with the later not being a W shaped dispersion.

Since the conduction direction z is infinite in length and we neglect electron scattering, one can assume the conductance electrons to conduct with a chance of unity. In this trivial regime electrons with Fermi momenta k_f and positive velocity contribute one conductance quantum, equal to $\frac{2e^2}{h}$ where h is the Planck constant times 2π, to the total conductance. One includes only the electrons with positive velocity because transport happens in the one direction and thus it is either left to right or vice versa, never both. The velocity of electron is the slope of energy dispersion $\frac{\partial E(k)}{\partial k}$. Thus one can write:

$$G = \frac{1}{2} \sum_i \frac{2e^2}{h} \left| \{ k_F \mid E(k_F) = E_F \} \right| , \tag{2.21}$$

where G denotes the conductance, fraction $\frac{1}{2}$ arises from the fact that crossing at Fermi level comes in pairs of positive and negative slopes (ofter called a conductance channel). $\{k_F \mid E(k_F) = E_F\}$ is the set of all momenta at the Fermi level and $|\cdot|$ is the size of this set.

Inspection of figure 2.2 grants insight into behaviour of conductance as a function of E_i. E_i doesn't change the shape of dispersion, instead it changes the position of the dispersion relating to E_F. Let E_i decrease starting from a value larger than E_F. The dispersion will continuously move down and bigger parts of it will be below the E_F. Due to different shapes of the dispersion the conductance, specifically the amount of energy crossing at E_F, will change. First dispersion, will have a conductance in the shape of $0 \rightarrow 1 \rightarrow 2$ for the red dispersion and shape of $0 \rightarrow 2$ for the green one. The factor 2 comes from energy degeneracy the green dispersion has. The size of 1 plateau scales linearly with E_Z. Second dispersion will go as $0 \rightarrow 2$ with the point where one goes to 2 will move down in energy linearly as a function of α. In the third plot the Fermi level inside of the Zeeman induced gap for some finite interval of E_i. Thus the conductance will go like $0 \rightarrow 2 \rightarrow 1 \rightarrow 2$ for the green conduction and red will behave exactly the same as in the first plot (even though $\alpha \neq 0$ there). Conductance of the green dispersion in a way special since intuitively one would expect conductance to be a strictly decreasing function of energy. The area where conductance drops is known as the helical gap and, just like W shapeddispersions, is the focus of this research. Tilted magnetic field changes the conductance even further. One half of W is lower for $\theta \neq 0$ and thus conductance will go like $0 \rightarrow 1 \rightarrow 2 \rightarrow 1 \rightarrow 2$. Vanishing of the Zeeman gap for $\theta = \pi/2$, will in turn close the helical gap.

To study this more, a relation between α and E_Z is derived, equalizing the size of energy gap caused by E_Z and the depth of the W shape created by SO coupling. This way one has maximum resolution when sweeping the energy scale. The equation reads:

$$E_Z = \frac{1}{6 + 4\sqrt{2}} \alpha^2 . \tag{2.22}$$

2.5 Constants and energy scales

This section gives numerical values for various constants and parameters used throughout the project. The effective mass of an electron m^* in Indium Antimonide (InSb) is 1.4% of electron mass m, with $m = 9.1\text{e}{-31}$ kg. The size of spacing in the equidistant grid denoted by a,is also often referred to as the energy hopping length and equals 2.5 nm. Thus the size of energy hopping t described in section 3.1.1 is $t = \frac{\hbar^2}{2m^* a^2} = 7\text{e}{-20}$ J. Energy units of t is the unit system used by the Kwant [9] package.

The Zeeman effect E_Z depends on the size of magnetic field, and in most practical purposes has a value in the range of $[0, 10]$ meV, corresponding to a range of $[0, 23]$ mt. The SO length parameter enters the calculations by stating $\alpha = \frac{2a}{l_{SO}}$. Typical values of l_{SO}, expressing the magnitude of α in equation (2.9) are in the range of $[50, 300]$ nm. This puts SO strength in the range of $[0.002, 0.1]$. If one still wants to observe W shaped dispersion, the parameter l_{SO} defines an upper-bound on E_Z. In order for $\alpha^2 > 4E_Z$ to hold, the range for E_Z used in this project becomes $[0, \alpha^2/4]$. Biggest Zeeman energy one can thus encounter is 2.5 mt.

The last energy parameter involved in equation (2.19), the eigenenergies E_i can take about any negative value, depending on applied voltage difference V_G. The relation between the two is highly non trivial as can be seen in the section results.

Values of ϵ used in equation (2.13) is 17.7 $\frac{\mathrm{F}}{\mathrm{m}}$ inside of the wire and 8.0 $\frac{\mathrm{F}}{\mathrm{m}}$ inside of the dielectric.

Another energy scale used in section 3.3 relates to temperature. Boltzmann constant k_B relates temperature T to energy by a simple relation $E = k_BT$. In units of t one Kelvin corresponds 0.2 mt. Temperature is a metric of average energy so due to inherent randomness of it one doesn't just introduce a temperature dependent term in the Hamiltonian.

Instead, one goes for more statistical approach by introducing the Fermi Dirac distribution as described in the (2.11). Figure 2.3 shows the relation between temperature and shape of this distribution. Observe how the distribution approaches a step function for $T \rightarrow 0$.

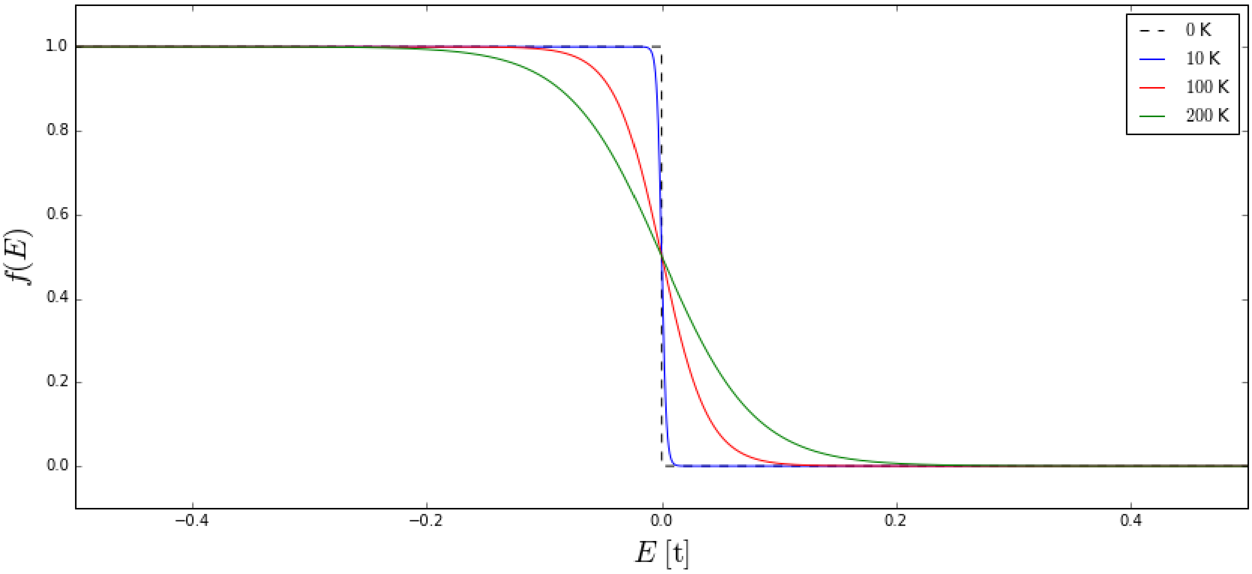

Figure 2.3: Fermi distribution plotted for few values of T.

Chapter 3

Numerical Model

3.1 Background

This work builds on a master project done by Adriaan Vuik [2]. The algorithms written by him solve the system for various strengths of SO coupling and E_Z, for magnetic field oriented along the nanowire.

Chapter 3.1.1 outlines the algorithm according to [2]. Introduction of tilt in the magnetic field direction θ forces one to invent a new way for the Density of States integration as explained in section 3.1.2. Anderson method described in Chapter 3.2 is used for major speed up of the calculations. Temperature annealing process has been introduced to fix a non-convergence issue caused by the van Hove singularities in the Density of States, see section 3.3.

3.1.1 Self consistent solution loop

Let $\phi_n(x_i, y_j)$ be the electric potential after n iterations. x_i, y_j denote coordinates in equidistant grid used for finite differences approximation of 2.18. Finite differences approximation states

$$-\frac{\hbar^2}{2m^*}\frac{\partial^2}{\partial x^2}\psi(x_i, y_j) \approx t(\psi(x_{i-1}, y_j) + \psi(x_{i+1}, y_j) - 2\psi(x_i, y_j)), \tag{3.1}$$

where $t = \frac{\hbar}{2m^* a^2}$ and $a = \Delta x$ the size of spacing between grid points. Physical interpretation of a is the size of energy hopping (see section 2.5). A similar equation can be written for the derivative with respect to y. Solving for the eigenenergies - eigenvectors of $H_{x,y}$ reads:

$$E_i\psi(x_i, y_j) = -e\phi_n(x_i, y_i) + t(\psi(x_{i-1}, y_j) + \psi(x_{i+1}, y_j) + \psi(x_i, y_{j-1}) + \psi(x_i, y_{j+1}) - 4\psi(x_i, y_j)). \tag{3.2}$$

Using those equations one can build a matrix describing the discretized operator $H_{x,y}$. This whole process is made very simple by the use of Kwant package [9]. Kwant allows users to define the geometry of a system and then defines a equidistant grid on it. Chapter 3.1.2 describes how the charge density ρ is calculated from the eigenenergies and eigenwaves of said matrix. One then translates charge density to the grid used for the Finite Elements Method. Grid points on the FEM grid are denoted by $\hat{x}_i, \hat{y}_j$.The Dolfin package [10] is used to solve equation (2.13) and thus obtaining a new electric potential $\phi_{n+1}(\hat{x}, \hat{y})$. Lastly, one transforms the potential back to the equidistance grid.

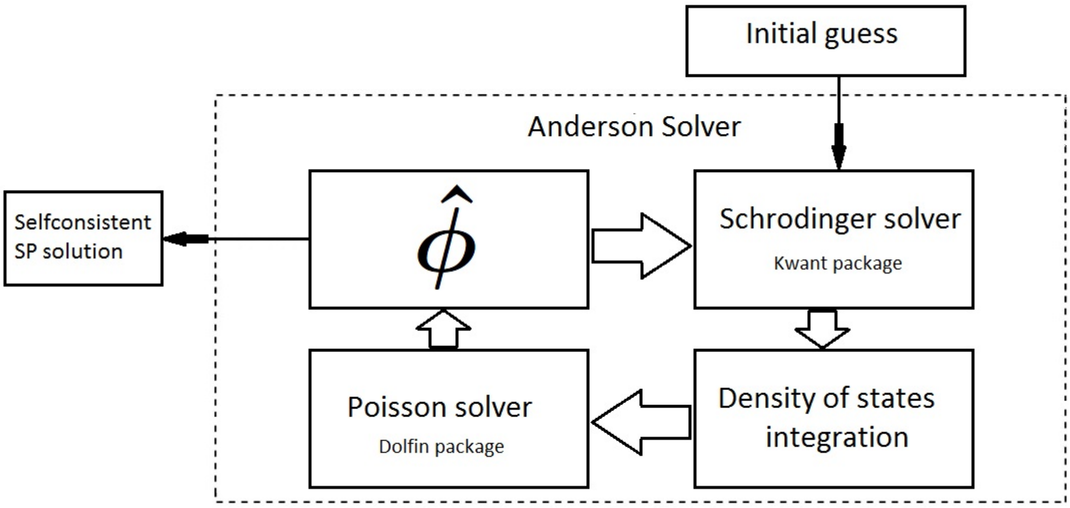

Figure 3.1: Schematic visualisation of self consistent solution loop. Anderson terminates when difference between last two iterations is smaller than some tolerance.

Pseudo Code

```
INPUT $\phi_n(x_i, y_j)$ DO:
$E_i$ , $U_i(x_i, y_j)$ = Kwant($H_{x,y}$, $\phi_n(x_i, y_j)$) (See (2.16))
$\rho(x_i, y_j)$ = INTEGRATE($E_i$, $U_i(x_i, y_j)$) (See 3.1.2)
$\rho(\tilde{x_i}, \tilde{y_j})$ = INTERPOLATE($\rho(x_i, y_j)$)
$\phi(\tilde{x_i}, \tilde{y_j})$ = Dolfin($\rho(\tilde{x_i}, \tilde{y_j})$) (See (2.13))
$\phi_{n+1}(x_i, y_j)$ = INTERPOLATE($\phi(\tilde{x_i}, \tilde{y_j})$)
OUTPUT $\phi_{n+1}(x_i, y_j)$
```

Iterations described in chapter operate on the electric potential ϕ instead of the charge density ρ. One might consider iteratively calculating new charge densities but previous research [3] shows that fix point iterations $\phi(\rho(\phi)) = \phi$ are better conditioned than it's counterpart in terms of ρ

The Picard iteration is fairly expensive to calculate, so one can use a more complex solver in order to significantly speed up the process. Anderson mixing scheme (see 3.2) performs best of the solver availible from SciPy [3].

3.1.2 Density of states integration

Consider Equation (2.12). Recall $D_i(E) = \frac{1}{2\pi}\frac{dk}{dE}$. Since SO coupling does not happen in the cross section, the eigenfunctions $U_{i,k}$ are not actually k dependent. Write $U_{i,k} = U_i$. One can thus simplify:

$$\rho(x,y) = \sum_i \int\limits_{E \le E_F} |U_i(x,y)|^2 \frac{1}{2\pi} \frac{dk}{dE} dE \tag{3.3}$$

$$= \frac{1}{2\pi} \sum_i \int\limits_{E \le E_F} |U_i(x,y)|^2 \frac{1}{2\pi} dk \tag{3.4}$$

$$= \frac{1}{2\pi} \sum_i |U_i(x,y)|^2 \int\limits_{E \le E_F} dk. \tag{3.5}$$

Note that since energy dispersion is not an injective function DoS is not a well defined function, and thus the last integral doesn't have a closed form solution. Naively one might want to invert (2.19) and simply evaluate it at E_F to find k_F and thus finding the upper and lower bound on the otherwise simple integral. Quick inspection of Figure 3.2 illustrates this problem. Imagine a horizontal line representing the Fermi energy. Moving this level up and down shows there are either 0, 4, 2 Fermi momenta k_F for which $E(k_F) = E_F$, in some cases such points are on entirely different branches of dispersion (referring to ± sign in the equations). It is noteworthy that in practice the Fermi level is set to zero, and the dispersion has a different offset E_i.

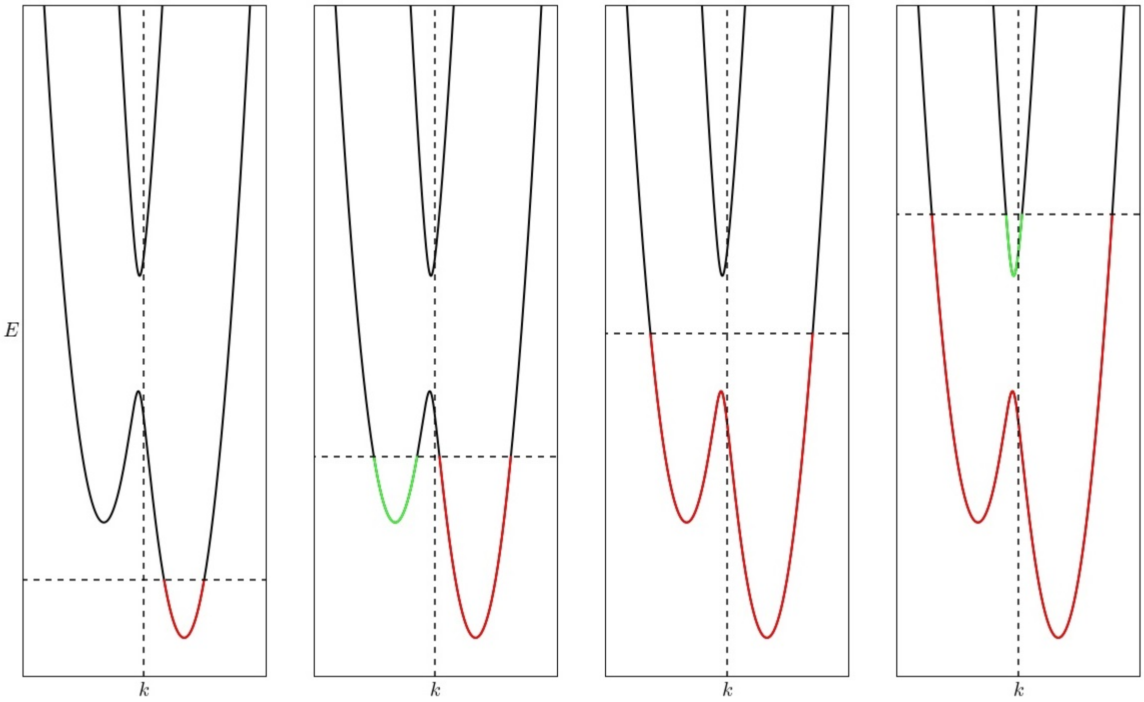

Figure 3.2: Schematic plots of W shaped energy dispersion for $\theta \neq 0$. Color lines describe part of the energy dispersion underneath Fermi level. This part is usually either not a connected set (2'nd plot) or some k values are used more than once (displayed right most).Note that this is one band case and in practice one might need to deals with many bands stacked above each other. This occurs when high energies are considered.

Thus, one needs to know where the Fermi level lies in relation to the energy dispersion. In order to do so, a numerical solver is used to determine the location of minima and maxima along the dispersion.

For the two minima's of the W-shape band Newton-Raphson method is used to determine the zero of a derivative of $E(k)$. The iterations read:

$$k_{n+1} = k_n - \frac{E'(k_n)}{E''(k_n)}, \tag{3.6}$$

with:

$$E'(k_n) = 2k_n - \frac{\alpha(\alpha k_n + E_Z \sin(\theta))}{\sqrt{(\alpha k_n + E_Z \sin(\theta))^2 + E_Z^2 \cos^2(\theta)}}$$
$$E''(k_n) = 2 - \frac{(\alpha E_Z \cos(\theta))^2}{(\alpha k_n + E_Z \sin(\theta))^2 + E_Z^2 \cos^2(\theta))\sqrt{(\alpha k_n + E_Z \sin(\theta))^2 + E_Z^2 \cos^2(\theta))}}$$

The iterations start at $k_0 = \pm M$ such that $E(M) >> E_F$. In practice, a value of $M = 10^6$ is sufficient. This calculation needs to be done only once instead of every iteration of the solver, so efficiency isn't the issue here. Rather convergence is essential.

Newton-Raphson will converge if $E''(k) \neq 0$ in the neighbourhood of the solution, and the initial guess is in this neighbourhood. Short inspection of $E(k)$ shows that $E'(k)$ has only three zeroes, and thus $E''(k)$ must have 2 zeroes. Yet, the dispersion behaves like a quadratic function for big k's, so one can assume the zeroes of $E''(k)$ to lie in between the minimum and maximum of the W shape (see Figure 3.2), and thus outside of the relevant neighbourhood of the local minimum.

When both minimas are found, the position of the maximum can be calculated using a bisection-like method, called Brent's method, to again determine the zero of $E'(k)$ in the interval $[k_{left} + \epsilon, k_{right} - \epsilon]$.

Brent is a combination of bisection, secant method and inverse quadratic interpolation [7]. We will use the notation from the same source to describe the algorithm.Let a, b be bounds of the interval and $f(a)f(b) \leq 0$, and $c = \frac{a+b}{2}$. If $f(a) = f(c)$ or $f(c) = f(b)$ the method takes a secant step:

$$x = b - f(b)\frac{b-a}{f(b) - f(a)} \tag{3.7}$$

Else, the quadratic interpolation is attempted. It reads:

$$x = \frac{[y - f(a)][y - f(b)]c}{[f(c) - f(a)][f(c) - f(b)]} + \frac{[y - f(b)][y - f(c)]a}{[f(a) - f(b)][f(a) - f(c)]} + \frac{[y - f(c)][y - f(a)]b}{[f(b) - f(c)][f(b) - f(a)]}$$

Setting y = 0 interpolates in the direction of the root and can be written as:

$$x = b + P/Q \tag{3.8}$$

where:

$$\begin{aligned}
R &\equiv f(b)/f(c) \\
S &\equiv f(b)/f(a) \\
T &\equiv f(a)/f(c) \\
P &= S[T(R-T)(c-b)-(1-R)(b-a)] \\
Q &= (T-1)(R-1)(S-1)
\end{aligned}$$

Either way, both iterations are expressed in the form of b plus some correction. If the correction were small or would put x outside of bounds or would be troublesome for numeric reasons ($f(b)-f(a)\approx 0$ or $Q\approx 0$), the method takes a simple bisection step instead.

The minimum of the upper-band of dispersion is also calculated using the Brent method, on the interval $[-M, M]$. With convergence of the method ensured, one needs also to ensure that the solution actually lies in the interval.

Again, quick inspection of the equation (2.19) shows that if the dispersion has a W shape then the local maxima will move between $[-\frac{E_Z}{\alpha}, \frac{E_Z}{\alpha}]$, same for the upper branch of dispersion. Thus, using $\pm M$ as bounds is fine.

Afterwards, one can calculate where the Fermi level lies with respect to dispersion. This knowledge is used to define intervals such that only crossing of Fermi level and dispersion lies in such an interval. Brent's method is again used, now to calculate the k of the crossing (reminder: E_F is set to 0, so the crossing happen at zeroes of the $E(k)$). Finally the integral term of (3.3) can now be computed and equals the total length of the interval underneath of E_F.

3.2 The Anderson algorithm

Anderson mixing scheme, also known as the Anderson acceleration method is an iterative zero point solver for nonlinear schemes that makes use of values obtained from previous iterations.

Let x_n be the nth output of Picard iteration described in 3.1.1 and f_n the function value (in this case it is the difference compared to last input to the Picard iteration). Let memory M be a collection of last solutions x and function values f. Define predictors $\bar{x}_n$ and $\bar{f}_n$, predicting the value of respectively the next solution and function value as:

$$\bar{x}_n = x_n - \sum_{i\in M} \gamma_i^n \Delta x_i = x_n - X_M \gamma^n \tag{3.9}$$

$$\bar{f}_n = f_n - \sum_{i\in M} \gamma_i^n \Delta f_i = f_n - F_M \gamma^n \tag{3.10}$$

where:

$$\Delta x_i = x_{i+1} - x_i \tag{3.11}$$

$$\Delta f_i = f_{i+1} - f_i \tag{3.12}$$

$$\gamma^n = (\gamma_{n-1}^n, ..., \gamma_{n-m}^n) \tag{3.13}$$

$$X_M = [\Delta x_{n-1}, ...\Delta x_{n-m}]^T \tag{3.14}$$

$$F_M = [\Delta f_{n-1}, ...\Delta f_{n-m}]^T \tag{3.15}$$

The weights for $\bar{x}_n$ and $\bar{f}_n$ are determined by the least squares estimation, minimizing the next function value:

$$\min_{\gamma^n} < \bar{f}_n, \bar{f}_n >= \min_{\gamma^n} |f_n - F_M \gamma^n|_2^2 \tag{3.16}$$

The normal equations of this condition read:

$$(F_M^T F_M)\gamma^n = F_M^T f_n \tag{3.17}$$

A new solution can be now calculated by:

$$\begin{aligned} x_{n+1} &= \bar{x}_n \\ &= x_n - X_M \gamma^n \\ &= x_n - X_M (F_M^T F_M)^{-1} F_M^T f_n \end{aligned}$$

One last improvement encountered in practice is the use of mixing parameter η, usually set to 0.5 [5]. This mixing introduces damping of oscillations in the solution. The final equation reads:

$$\begin{aligned} x_{n+1} &= \bar{x}_n + \eta \bar{f}_n & (3.18) \\ &= x_n + \eta f_n - (X_M + \eta F_M)\gamma^n & (3.19) \\ &= x_n + \eta f_n - (X_M + \eta F_M)(F_M^T F_M)^{-1} F_M^T f_n & (3.20) \end{aligned}$$

In practice Anderson iterations will continue, until $|f_n|_2 <$ tol where tol is usually about 10^{-5}.

A very natural connection to be made here concerns GMRES methods. Chapter 2.1 of [5] proves that Anderson has the same converging behaviour as GMRES for linear systems.

3.2.1 The memory

Great advantage of keeping an memory is quicker convergence compared to other methods [3], especially in cases where repeated computation of $f(x)$ is expensive [5]. Yet, clearly without an upper-bound on the size of the memory evaluation of Equation (3.18) will get expensive too (note that one needs to calculate the product of an M by n matrix with an n by M matrix). A more important problem arises from the fact that the solution tends to get better after more iterations, and a solver with big memory, keeps the old "bad" solutions in their calculations. For this reason M is often set to 2 [6] in practical applications.

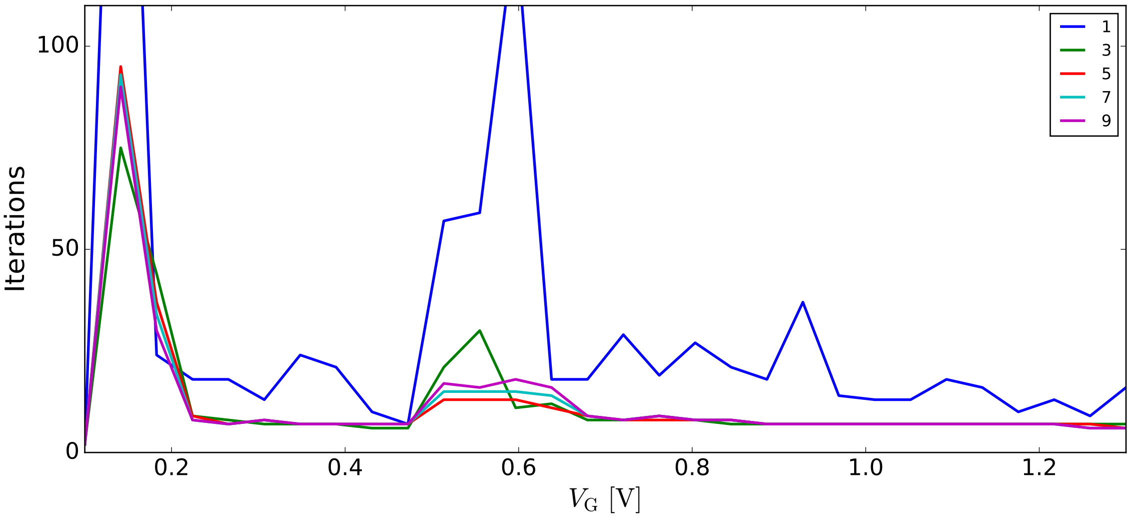

Figure 3.3: Few simulations with different values for M in $[1, 9]$

Figure 3.3 is a benchmark of amount of iterations needed for convergence versus gate voltage V_G. Each line corresponds to a different amount of solutions stored in memory. The base case of $M = 1$ performs significantly worse across the whole range of V_G. Other values for memory differ mostly in the area close for the first energy crossing. Those points have proven to be a strain on the solvers ability to converge, see section 3.3. For practical use, $M = 5$ has been used throughout the project.

3.2.2 Mixing parameter

While, the mixing parameter η is traditionally set to 0.5, this exact value is supported by only hand-waving arguments. Some authors [5],[6], actually propose values of η slightly lower than 0.5 to improve the convergence speed. Figure 3.4 shows that, indeed, the mixing parameter η has an effect on the amount of iterations needed in order to achieve convergence,especially around values at the two clearly visible peaks around $V_G = 0.17$ and $V_G = 0.5$. Yet, this isn't a clear trend as can be seen in Figure 3.5. There isn't clear neighbourhood in which value of η can be crowned as the optimal. On average, the exact choice of η doesn't matter much. One should note that few points that do require way more iterations on average are much less common than points where Anderson performs within acceptable bounds for $\eta = 0.5$. Lastly, figure 3.6 disproves the claims about η slightly lower than 0.5 being the optimal value. The general area close to 0.5 performs slightly better than the other values (about 11% better in the area $\eta < 0.5$ and even more on the other side, yet one can't point at a specific value and be sure that it performs the best.

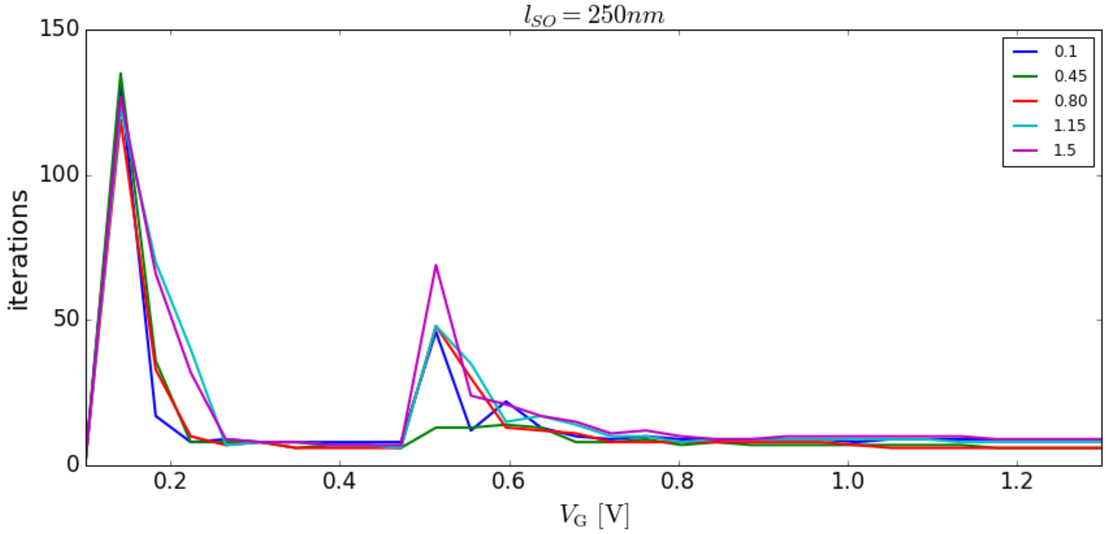

Figure 3.4: Large amount of simulations with different values of η in range $[0.1, 1.5]$. The amount of iterations needed for convergence is displayed against V_G.

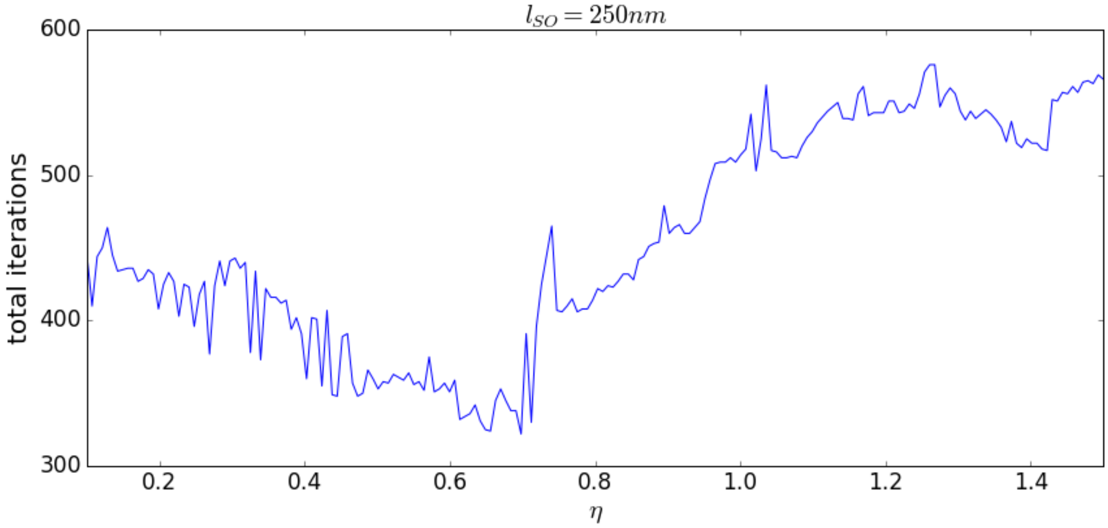

Figure 3.5: Large amount of simulations with different values of η in range $[0.1, 1.5]$. The total amount of iterations in V_G sweep needed for convergence is displayed against η.

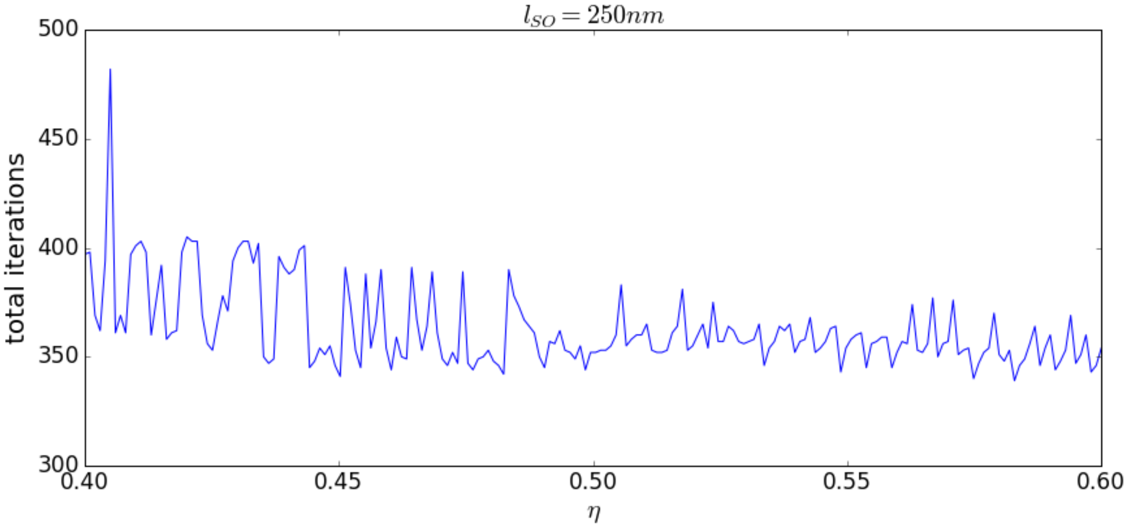

Figure 3.6: Large amount of simulations with different values of η in range $[0.4, 0.6]$. The total amount of iterations in V_G sweep needed for convergence is displayed against η.

3.2.3 Convergence analysis

The Anderson algorithms operates on the difference between the iterations as a metric for the ”quality” of solution. Since we are dealing with a fix point iterations this is a fine metric, in the sense that if $|f_n - f_{n-1}| < \epsilon$ where f_n is the solution and n iterations and ϵ is small then f_{n-1} should be fairly close to the actual fixed point f. Yet, this approach gives no insight into how the solution will improve as more iterations are calculated. To gain this insight one can analyse the K values relating the residuals of two consecutive iterations.

Say the residual of Anderson iteration obeys $|f_{n+1} - f_n| \leq K|f_n - f_{n-1}|$ for some constant $K \in \mathbb{R}$. Consider, two iteration steps n and m with $m > n$. Then one can write:

$$\begin{aligned}
|f_m - f_n| &\leq |f_m - f_{n+1}| + |f_{n+1} - f_n| \\
&\leq |f_m - f_{n+2}| + |f_{n+2} - f_{n+1}| + |f_{n+1} - f_n| \\
&\leq |f_m - f_m| + \sum_{j=n}^{m-2} |f_{j+1} - f_j| \\
&\leq \sum_j K^j |f_{n+1} - f_n|
\end{aligned}$$

If we now let $n \to \infty$ then the last line converges for K strictly lower than 1. Common method to prove convergence of a numerical method is to define $K_n = \frac{|f_{n+1} - f_n|}{|f_n - f_{n-1}|}$ and observe what the maximal value of K_n is for a finite amount of iterations. Simple Picard methods can relate the value of K_n to derivitive of function f close to the convergence point. Methods iterating on linear equations can often define some upperbound based on the equations to bound K_n. Equation (2.20) isn’t linear and Anderson isn’t a linear solver so one is left with observing the values of K_n.

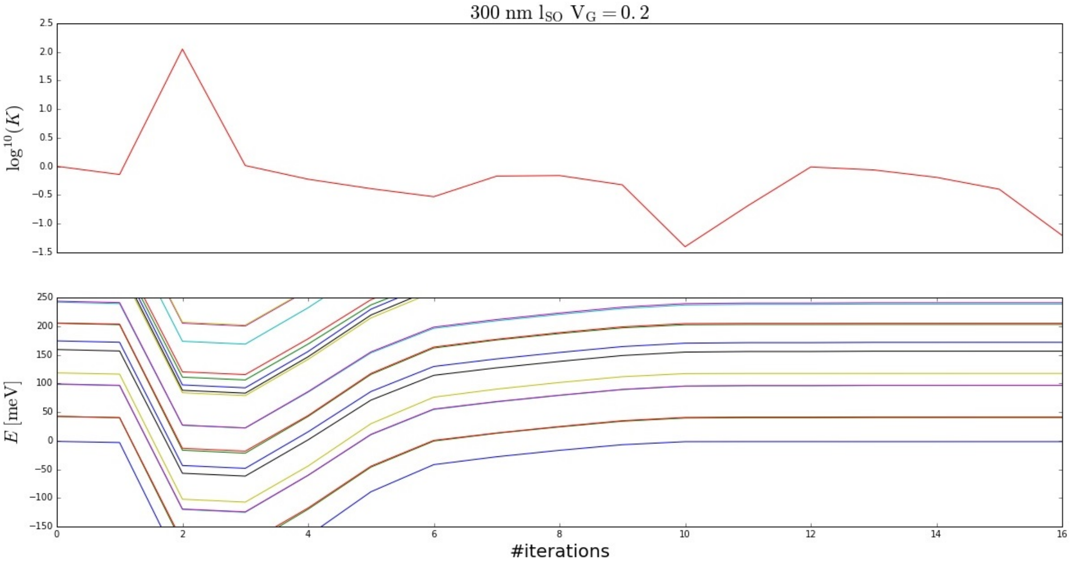

Figure 3.7: The upper plot is the value of K for every Anderson step needed for convergence. For this V_G the convergence isn't hard to archive as it doesn't lie close to a zero crossing. The lower plot denotes the energies E_i at every iteration.

Figure 3.7 shows the value of K_n for Anderson iterations until convergence has been reached. Energy levels at given iteration are displayed as an aid in understanding what is going on. At step 2 the algorithm made a huge correction to the energies, resulting in $K_2 = 110$. Other values of K_n are slightly lower than 1. Energy crossing (with zero) are hard for Anderson for reasons described in section 3.3, yet Anderson converged in just 16 steps. Figures 3.8 and 3.9 show similar peaks in K_n, also related to energy crossing. General trend can be observed that $K_n = 1 - \epsilon$ with $\epsilon \approx 10^{-4}$ unless Anderson tries to put energy levels below the Fermi level, in which case the value of K changes rapidly, often accompanied by a oscillation afterwards, as Anderson tries to find out how low the energies should be.

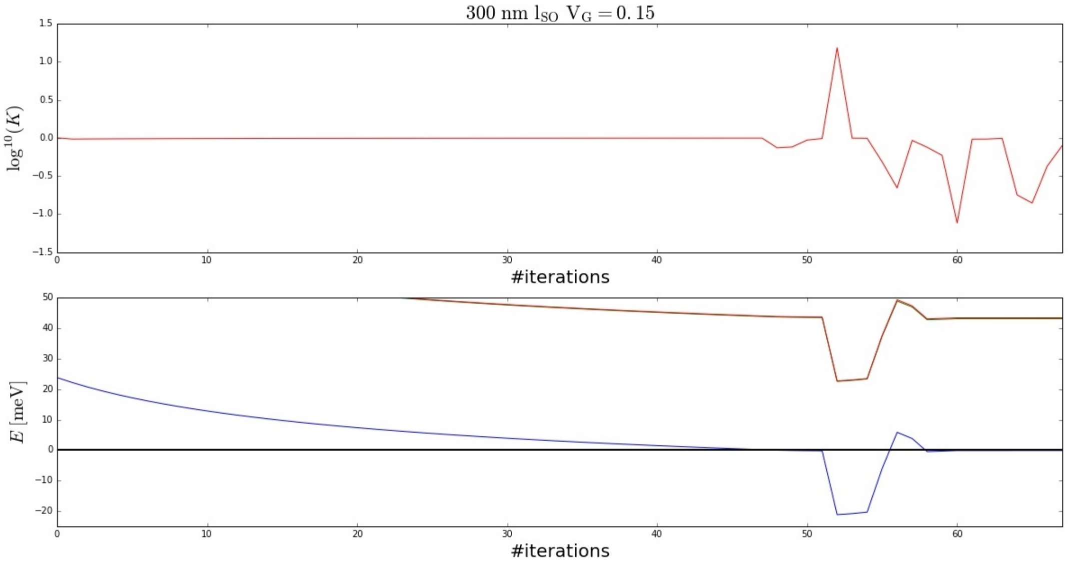

Figure 3.8: The upper plot is the value of K for every Anderson step needed for convergence. The lower plot denotes the energies E_i at every iteration. Here the final solution has energy levels close to zero, resulting in a much harder problem for Anderson.

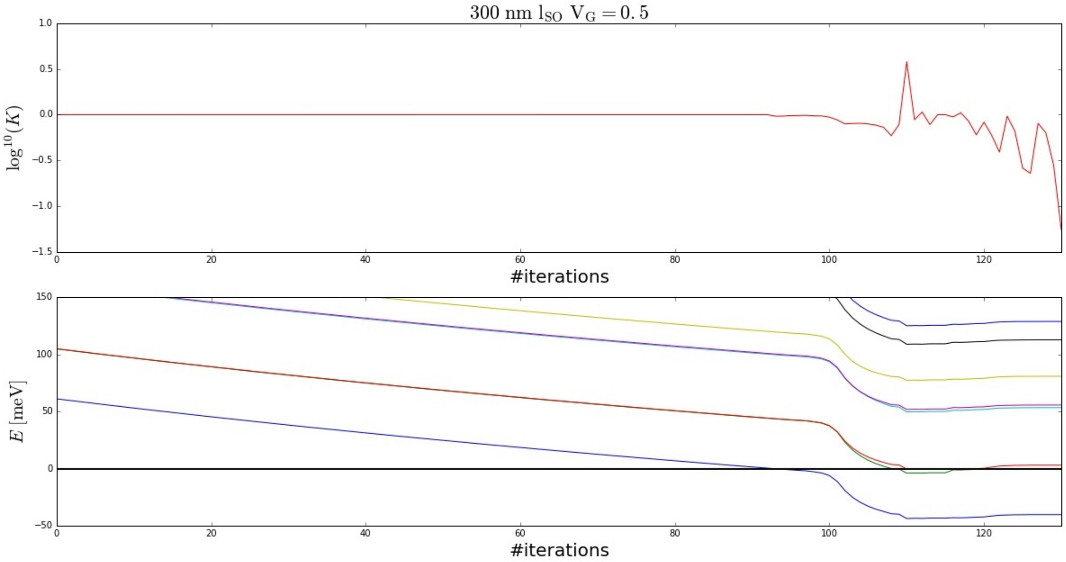

Figure 3.9: The upper plot is the value of K for every Anderson step needed for convergence. The lower plot denotes the energies E_i at every iteration. Observe how first and second excited energy (red and green line) are almost degenerate and both end up close to zero. This poses a much harder problem for Anderson than previous ones.

K analysis gives us some insight into general behaviour of Anderson scheme but one can't derive convergence from it. The oscillations in K and the tendency to remain very close to 1 all the way to convergence render this approach not useful. Anderson solver has the tendency to converge in "jumps" or "burst". Also we can't use it for to give any meaning full bound on the error made by Anderson.

3.3 Van Hove singularities nonconvergence

Consider equation (2.19), for E_i such that the lowest point of dispersion is larger than zero. Then there exists no k such that $E(k) = E_F$ and thus $D_i(E) \equiv 0$. As a result density in equation 3.3 equals zero. Then, if E_i gets pushed down just slightly then suddenly a part of the dispersion is below the Fermi level. Note that every band bottom starts with a local minimum and thus $\frac{dE}{dk} = 0$ there. This has a great effect on the density of states $D_i(E)$ as $\frac{dk}{dE} \to \infty$ on those points. Those points are referred to as Van Hove singularities named after Belgian physicist Leon van Hove [8].

Consider now the case for which α and E_Z are both zero and $E_i < E_F$. Then, the energy dispersion 2.19 is a simple relation $E = k^2 + E_i$ and thus $\frac{dk}{dE} = \frac{1}{\sqrt{E-E_i}}$. Integration yields:

$$\begin{aligned}
\int\limits_{E \leq E_F} D_i(E)dE &= \frac{1}{2\pi} \lim_{t \downarrow E_i} \int\limits_{E'}^{E_F} \frac{1}{\sqrt{E - E_i}} dE \\
&= \frac{1}{\pi} \lim_{t \downarrow E_i} \left(\sqrt{E_F - E_i} - \sqrt{t - E_i} \right) \\
&= \frac{1}{\pi} \sqrt{E_F - E_i},\ E_F = 0 \to \\
&= \frac{1}{\pi} \sqrt{|E_i|}.
\end{aligned}$$

This tells us two things: first, the integral over the singularity is finite, second the density (the integral) grows rather slowly as E_i gets more and more negative. Furthermore we can conclude that most of the density is at the bottom of a dispersion band. A similar argument holds for cases where the parameters are nonzero, with the small difference that DoS is defined starting from energies lower than 0 when E_Z is present. Figure 3.10 explores this. Dotted lines describe offset energy corresponding to minimas and maximas of energy dispersion being close to the Fermi level.

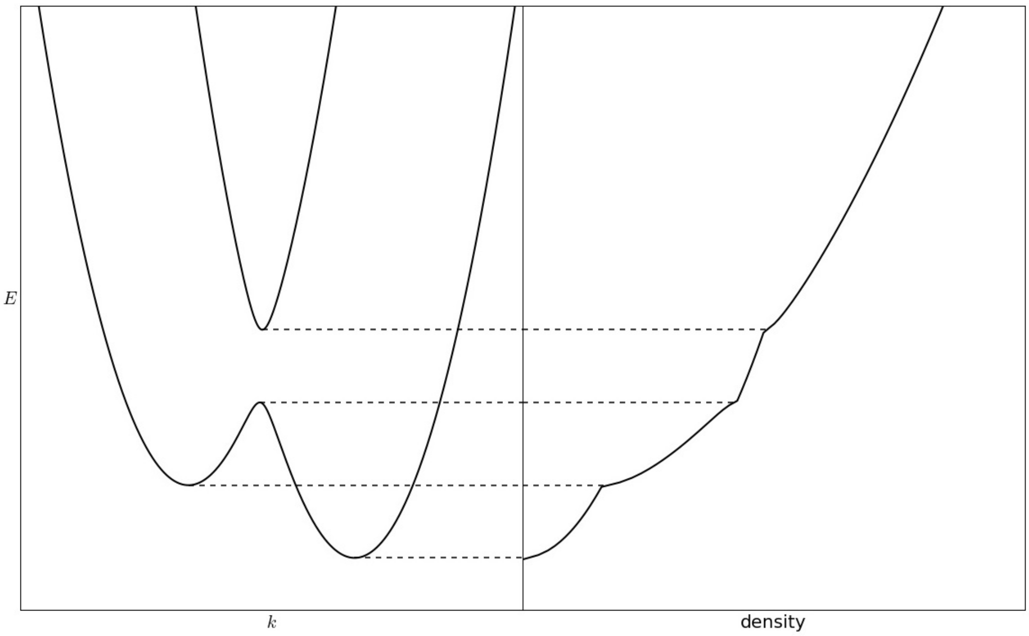

Figure 3.10: Schematical display of energy dispersion and corresponding density. Dotted lines stand for different Fermi levels. Note the kinks in density at the heights of minima and maxima of dispersion.

This is somewhat troubling for the solver, as when $E_i \approx 0$ then small change in E_i can force a big change in the density, and by extension in the electric potential. Anderson, being an iterative solver can be forced to oscillate between electric potential resulting in E_i just above zero and electric potential resulting in E_i just below the zero. Those aren't actually oscillation as Anderson is a quite robust solver, yet it forces the convergence speed to be painfully low, to the point that the amount of iterations needed for convergence makes the problem to be practically unsolvable.

Solution to this issue is the introduction of the temperature T back into the equations, to smooth out the kinks in the density. The same steps are taken as in section 3.1.2 regarding $U_{i,k}$ resulting in:

$$\rho(x,y) = \sum_i |U_{i,k}(x,y)|^2 \int_{-\infty}^{\infty} F(E, E_F, T)\frac{1}{2\pi}\frac{dk}{dE}dE \tag{3.21}$$

$$= \frac{1}{2\pi}\sum_i |U_{i,k}(x,y)|^2 \int_{-\infty}^{\infty} F(E, E_F, T)\frac{dk}{dE}dE \tag{3.22}$$

$$= \frac{1}{2\pi}\sum_i |U_{i,k}(x,y)|^2 \int_{-\infty}^{\infty} F(E(k), E_F, T)dk, \tag{3.23}$$

where, F stands for the Fermi Dirac distribution introduced in section 2.3. Shape of F for various temperatures can be seen in Figure 2.3 for various values of T.

Again, one can't naively integrate over k from $-\infty$ to $+\infty$. DoS has different branches, all of which need to be taken into account. Furthermore, F is a decreasing function of energy, and after $E = E_F$ the function starts to drop exponentially (see section 2.5), so we only need to integrate up to some finite energy only. For $E \geq E_F$ we have $F \approx \exp(-\frac{E}{k_B T})$, and at $E_{bound} = 100 k_B T$ we have $F(E_{bound}, E_F, T) \leq \epsilon_{machine}$. Thus, one defines bounds on the integral in the same way as in section 3.1.2 with the difference that $E(k)$ is first shifted down $100 k_B T$ to ensure $E(k_{bound}) = 100 k_B T$. Then integration of F occurs using the trapezoidal method. Figure 3.11 explores the results for various temperatures.

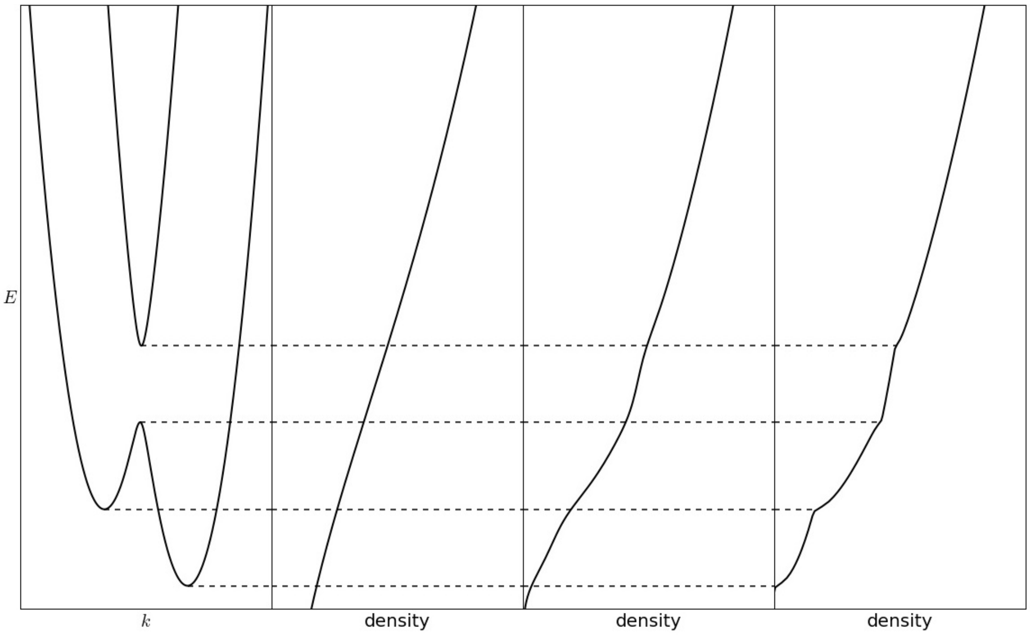

Figure 3.11: Schematic display of energy dispersion and corresponding density for nonzero temperature. Dotted lines stand for different Fermi levels. Temperature goes from 10 K to 0.1 K in logarithmic steps. Note the disappearance of kinks in the first plot.

Increased smoothness of density vastly increases the convergence speed for the Anderson solver. One can thus solve the system for some T_n, resulting in ψ_{T_n}. Afterwards this solution can be used as initial guess in order to solve the system for some lower T_{n+1}. This process is known as temperature annealing, and is repeated until $T_n \approx 0$. Temperature annealing can be more expensive to use than straight forward approach yet it can improve the initial guess for $T = 0$ ensuring convergence close to the van Hove singularities. Lastly, note how the last density plot for $T = 0.1$ resembles density for $T = 0$. If Anderson fails to converge even with the use of temperature annealing one might be satisfied with ψ_{T_n} if $T_n \approx 0$. 1 mK is small enough for all practical purposes (see chapter 2.5).

3.3.1 Temperature range optimization

Temperature steps used in the process of annealing have huge impact on the speed of the process (and in some cases also on whether or not the Anderson solver converges). The natural choice of steps are logarithmic as opposed to linear to ensure linear changes of the Fermi Dirac distribution between annealing processes. This helps to ensure the solutions be close to each other.

Temperature annealing is a process used only when Anderson solver fails to converge on its own. In order to test it, a V_G range was found with an energy crossing in it. The corresponding van Hove singularity (see chapter 3.3) makes it very hard for Anderson to converge. In this range few annealing ranges have been tested. Figure 3.12 is a test of few different ranges. The goals is to optimize convergence close to energy crossing (as seen in the lowest plot), in an area when Anderson performs poorly. Note that when using the solver in practical cases, one expects a solution in less than 300 iterations, where for every new temperature the counter resets to zero. Value of 2000 iterations corresponds to computations not converging. Baseline plot, has a peak around the area with energy crossing the zero (see the lowest plot). Big change in charge density and resulting discontinuity have big impact on the solver. In the first plot the linear ranges failed to converge thus, one can conclude, that linearly spaced ranges are bad for annealing.
Second plot displays the logarithmically spaced ranges. Two of those ranges do converge quicker than the baseline, a very nice result, proving the use-fullness of temperature annealing.
The ranges displayed in 3rd plot fulfil practical expectations as here one can observe that all the ranges were an improvement on the no annealing case. Each range has a lower lower bound than the previous one with fixed (19) amount of steps. Not surprisingly range corresponding to the highest lower bound converged in least amount of steps. One can observe that outside of general neighbourhood of a energy crossing, all the annealing ranges performed worse than the baseline. For this reason it is not ad viced to use temperature annealing except for proximity to energy crossings. It is thus advised to use logarithmically spaced temperature ranges, with the highest temperature around 100K, in order to easily converge when operating on an initial guess. That way next iterations can use previous result as a initial guess, which usually improves the convergence rate by quite a bit. 19 steps seems to be the right trade off between the amount of iterations needed and stability. Lastly an upper bound of about 0.01 K is sufficient for all physical purposes.

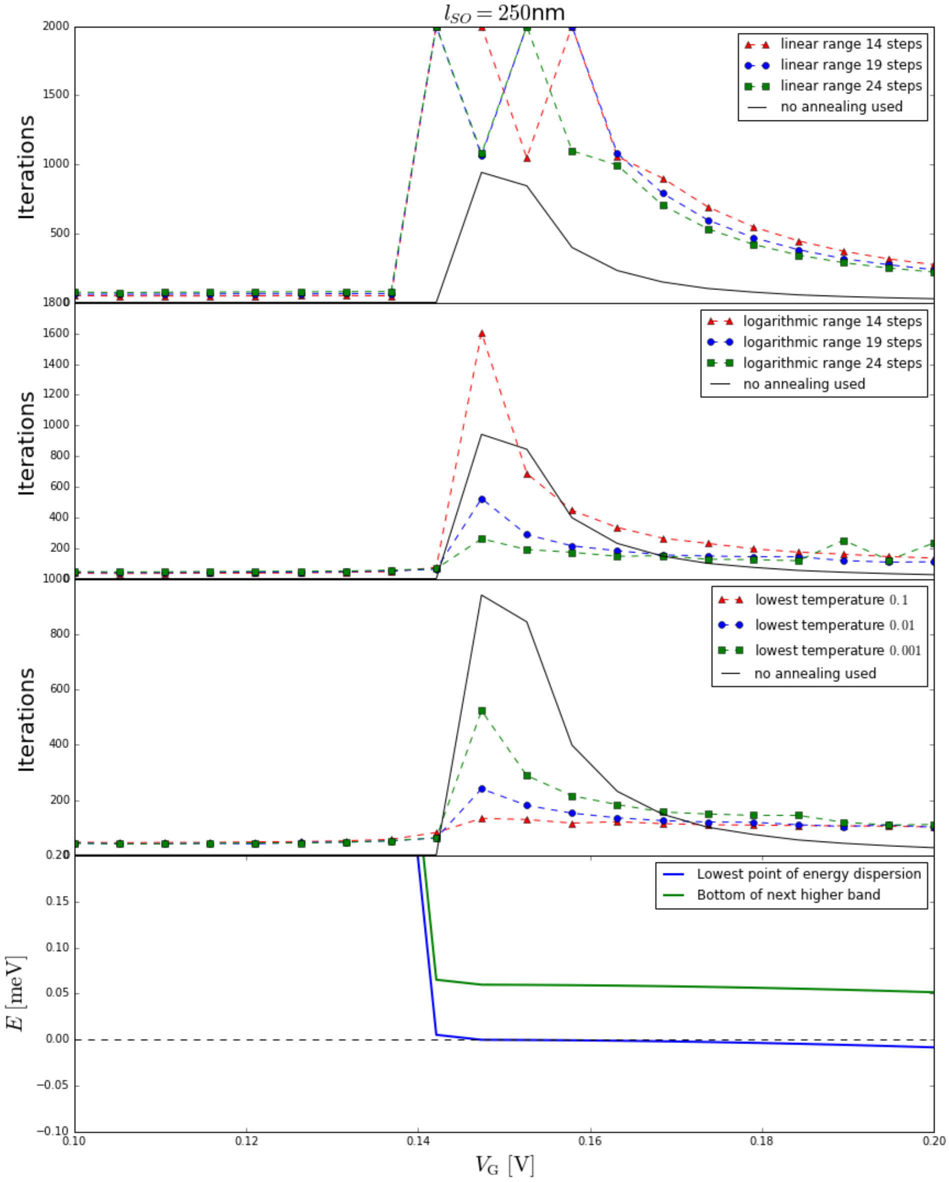

Figure 3.12: 3 graphics of number of Anderson iterations needed for each V_G in the sweep and energy levels displayed as a function of V_G. In the first plot, 3 linearly spaced temperature ranges of $[100, 0.01]$ K were used. All three of those ranges failed to converge within the fixed set of steps. Next plot displays logarithmically spaced ranges of $[100, 0.001]$ K. The amount of temperature points inside the range has been changed from curve to curve. All 3 converged, and ranges with 19 and 24 steps managed to do so in less steps than the baseline plot. Last 3 ranges all have 19 elements, and the lowest temperature is varied between 0.1 to 0.001.

Chapter 4

Results

In this section, the relation of electrostatics on energy as a function of gate voltage V_G is displayed for the first few bands of dispersion. This allows us then to show a more realistic relation between conduction and gate voltage V_G. A theoretical phase plot, displaying conduction as a function of the direction of magnetic field θ and energy, is shown next. Scaling properties of two conduction regions are researched for fixed spin orbit strength and changing Zeeman energy E_Z. Main focus is the helical gap introduced in chapter 2.4,the other region arises only for $\theta \neq 0$. A phase plot of conduction, now in terms of θ and V_G is analyzed, calculated using maximum resolution relation between α and E_Z from chapter 2.4. Lastly, we look at a conduction plots for varying strengths of magnetic field. This is done for 4 different directions of the field, respectively $\theta = 0,\ \pi/4,\ \pi/3$.

4.1 Energy and electrostatics

Solutions to the SP equation can be expressed in terms of electrostatic potential, charge density or eigen energies E_i together with the eigen waves. While, E_i's on it's own don't fully describe the system they are a useful resource for understanding general trends in the system. Figure 4.1 is a display of the lowest 9 eigenenergies as a function of gate voltage V_G. One can see that whenever a E_i crosses the Fermi level all curves have a kink. This phenomena corresponds to the van Hove singularity, where E_i crossing the E_F suddenly adds lots of density to the system. The spacing between energies isn't constant. Most notably the first and second energies are degenerate up to the point where the ground state E_0 crosses the E_F and by doing so puts the first electrons in the system. Most likely, this energy degeneracy is due to some rotational symmetry the wire has. Electrostatic field, not sharing the symmetry, breaks the energy degeneracy.

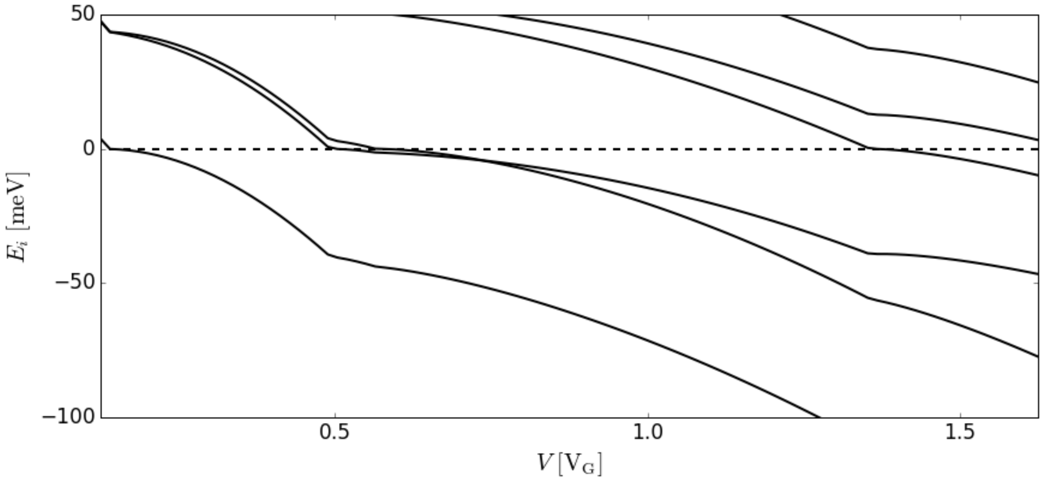

Figure 4.1: Plot of the lowest 6 eigen energies E_i of a global back gate device. The dotted line represents the Fermi energy E_F. Parameters used here are: $l_{SO} = 250$nm and $E_Z = 0.014$ meV.

For practical purposes, the energy scale is fairly big - usually one wants to measure the ground state only. Thus in next section we only look at a smaller range of V_G.

4.2 Conductance and direction of magnetic field

To test the conductance behaviour, mainly the existence and size of helical gap for various θ, one can artificially sweep the E_i parameter. Figure 4.2 explores this idea. Length of spin-orbit interaction has been chosen to be 250 nm for this calculation. The corresponding E_Z has been calculated for a maximum resolution, see section 2.4. As a result, for $\theta = 0$, the size of helical gap (starting at around -0.03meV) corresponds to the size of conductance of two area. Other noteworthy features are: the fact that, for higher θ the phase transition of $0 \to 1$ happens at a lower energy (due to deeper W shape) and closing of the helical gap for $\theta = \pi/2$. These phenomena are to be expected as seen in chapter 2.4.

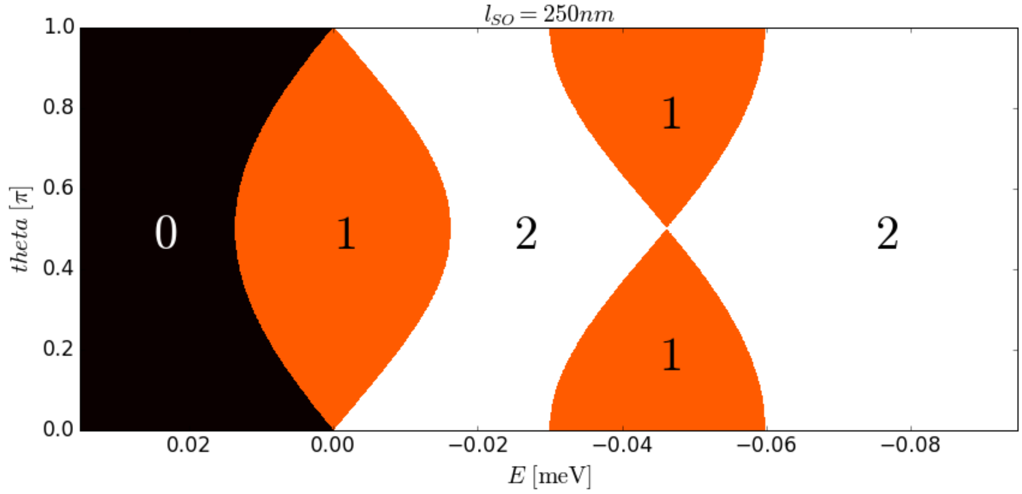

Figure 4.2: Phase plot of the conductance against E_i and angle of magnetic field θ. Colors denote the amount of conduction channels see section 2.4. x axis is the energy of lowest point of dispersion for $\theta = 0$, lowered not only by E_i but also by E_Z and SO coupling. Calculations have been only done for $0 \leq \theta \leq \pi/2$ as, due to the symmetry, one can copy the data over.

For practical purposes a better way to describe conductance is based on gate voltage V_G. Figure 4.3 is the conductance calculated through out a V_G sweep, for θ fixed to zero and $l_{SO} =$ 50nm.

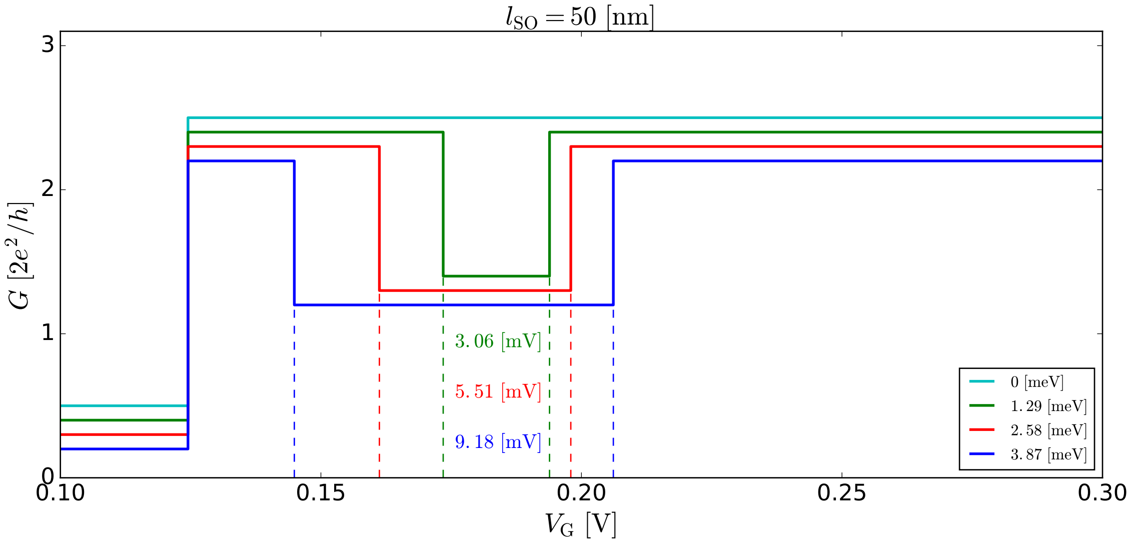

Figure 4.3: Conductance vs V_G for $\theta = 0$. Various Zeeman energies in range of $[0, 4]$ meV are plotted, each was given an offset to make features more visible.

Various values of E_Z are plotted and the helical gap appears for nonzero E_Z. One can observe how the size of the gap scales almost linearly with Zeeman energy. This is a well understood phenomenon. Whilst in the gap contribution to charge density comes mostly from the k^2 term of energy dispersion (as the dispersion is approximately parabolic there). Thus, similarly to the example used in the section 3.3, ΔE change of energy will cause an $\int\limits_{E}^{E+\Delta E} \frac{1}{\sqrt{E}} dE$ change in charge density, where $E > 0$. The helical gap contributes close to nothing to the charge density, thus charge screening stays roughly constant in the system. Similar arguments can't be made if the system is in first conductance one phase. Figure 4.4 used the same set of parameters, now for $\theta = \pi/2$. Here the lower conductance area comes from the uneven W shape caused by θ. Here the scaling isn't linear anymore. In this phase, any charge added to the system has a significant influence on charge screening, and thus on the relation between energy and V_G.

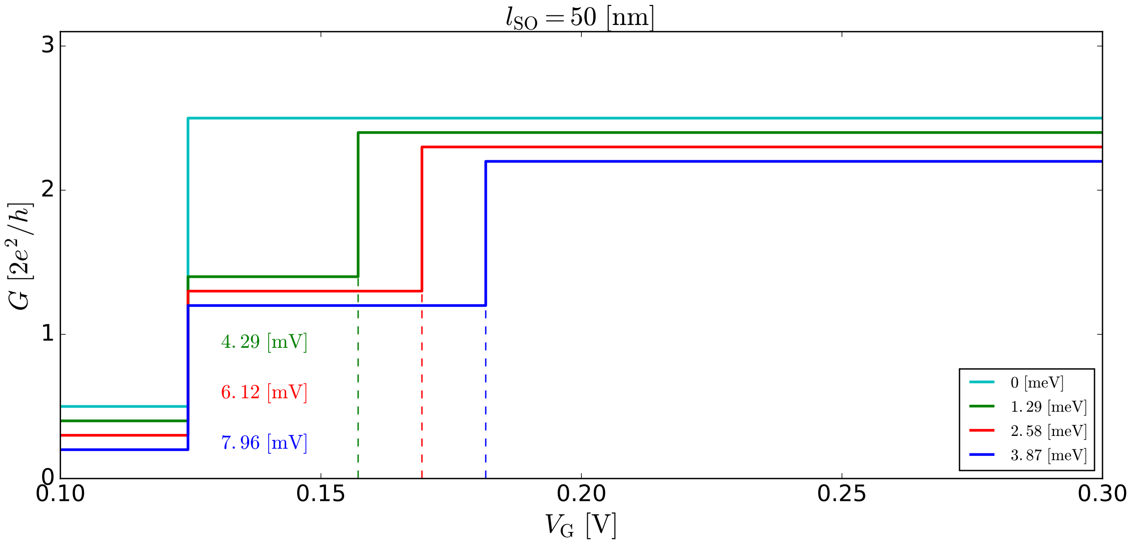

Figure 4.4: Conductance vs V_G for $\theta = \pi/2$. Various Zeeman energies in range of $[0, 4]$ meV are plotted, each was given an offset to make features more visible.

Figure 4.5 is vastly different from it's predecessor, and displayed energy levels help to understand the difference. Firstly, there are clear area's where Anderson solver had trouble converging, which can be related to the big change in charge screening. Conductance transitions occur at the points of the van Hove singularities (see section 3.3) in energy dispersion. The first transition, $0 \rightarrow 1$ is harder for the solver compared to $2 \rightarrow 1$ transition of entering the helical gap. In the 0 conductance area there are no electrons in the system yet, resulting in no density. This causes the E_i to change rapidly as a function of V_G, specifically the change is 3 orders of magnitude higher than for any other V_G. Resulting kink (discontinuity in the derivative) in the energy curve is harder to converge around than the kink corresponding to $2 \rightarrow 1$. For this reason, points for which Anderson fails to converge by the use of temperature annealing, fail at higher temperature compared to failure points close to $2 \rightarrow 1$ transition. This point can be made stronger by noting that the kink related to leaving the helical gap ($1 \rightarrow 2$ transition) doesn't create any trouble for the temperature annealing aided convergence, as seen by the lack of white dots in that area.

Secondly, shape of transitions has changed as compared to previous plot. First transition has now a flat sharp edge instead of egg like feature in the figure 4.2. One can explain this phenomena by again referring to rapid change of E_i in the 0 conductance phase. This requires one to have a immensely high resolution in V_G parameter to observe more rounded up edge. Specifically, the shape of transition can be approximated to be symmetric in energy, and for $\theta = \pi/2$ conductance of 1 region stretches for 4.8 mV corresponding to energy of 7.4 μeV. On the 0 conductance side this would correspond to voltage resolution of 7.4 nV. Appendix C zooms in on this issue.

Energy change throughout the V_G range stays roughly linear through the corresponding phase. One can observe that inside of the helical gap the energies change more than outside of it. The red energy line corresponding to $\theta = \pi/2$ is far from being a straight line in conduction of 1 phase.

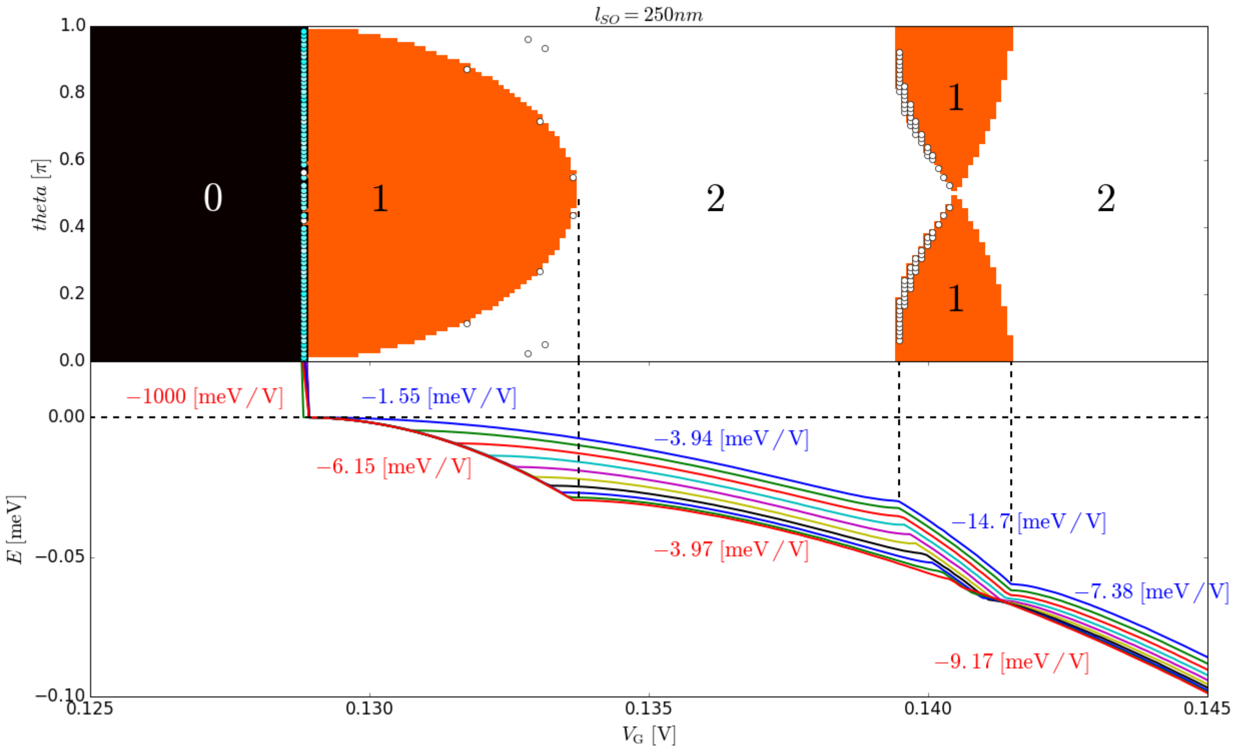

Figure 4.5: Phase plot of conductance against gate voltage and angle θ. Dots represent point where temperature annealing failed to converge, and result for finite temperature had to been used in the range of 0 to 90 mili Kelvin. White color corresponds to lower temperature.Lower figure is a plot of lowest point of energy dispersion for few different angles of θ. Helplines are drawn to further display the relation between energy and conductance. Colored numbers describe an average change of E_i as a function of gate voltage in the area between dotted lines, blue corresponding to $\theta = 0$ and red to $\theta = \pi/2$. Again, the data has been only calculated for $0 \leq \theta \leq \pi/2$ and copied over.

4.3 Conductance and the magnitude of magnetic field

This section takes a similar approach as the previous one. This time the magnetic field is changed and the direction of it stays set. First, E_i is artificially swept in order to give an expectation of the shape of the conduction. Then the conductance is calculated as a function of V_G. Lowest point of energy dispersion is plotted along as a function of V_G to help understand the changes in conductance.

Figure 4.6 displays the case for $\theta = 0$. The size helical gap scales approximately linearly with the Zeeman energy as expected from figure 4.3. Again, the $0 \to 2$ step has a sharp edge in terms of V_G instead of expected half circle. Lastly one can observe the effect helical gap has on the energies. While inside of the gap the energies drop quicker as a function of V_G.

Figure 4.7 is the case of $\theta = \pi/4$. Here, one expects the conductance to go as $0 \to 1 \to 2 \to 1 \to 2$ for nonzero E_Z. Specifically the size of the helical gap and lower conductance area due to the tilt in magnetic field is exactly the same size in energy. In terms of V_G this balance is broken, due to the charge screening. Another feature the system has is the small change in E_i in the area 2 conductance area left of the helical gap. Numerical artifacts can be seen for the highest E_Z in the middle plot. First, one can observe the conductance to remain at 1 while it shouldn't. For high E_Z the energy dispersion has a saddle point instead of minima-maxima-minima shape. When approaching this shape, the algorithms calculating the position of extrema simply run in into round off errors. Since those positions are crucial for calculation the density those small mistakes can have a huge impact on the E_i. This can be seen just right of 0 zone, where few points failed to converge at $T = 0$ causing a huge difference in the energy.

Lastly figure 4.8 gives us some insight into change of the relation between the size of conductance 1 area due to tilted dispersion and the size of helical gap. Here we consider the case of $\theta = \pi/3$. To avoid distracting numerical issues the size of E_Z range has been lowered slightly. One can observe that area corresponding to conductance of 1 due tilted dispersion stays roughly the same as in figure 4.7 in the V_G range. The helical gap on the other hand decreases. This trend will continue all the way to $\theta = \pi/2$ at which point the gap will disappear. Another feature is this: E_i is more flat in the area of conductance of 2 left of helical gap as compared to the $\theta = \pi/4$ case.

Electrostatics changes the scaling properties of the conductance plateau's. One can use it to the advantage, when determining whether or not the system is inside of the helical gap for given V_G. In practice, when magnetic field isn't perfectly aligned with the nanowire one can assume (for example by only doing conductance measurements) to be inside the helical gap while, in fact the system is in the first plateau related to tilted W shape of energy dispersion. This can happen quite easily as the first plateau takes more space up in the V_G domain as a function of E_Z. Sweeping the θ parameter won't directly characterize the area as the helical gap when it disappears for some value of θ, since the energy dispersion is perfectly W shaped for $\theta = 0$ thus the first plateau will disappear as well for some single value of θ. Instead, one can look for scaling laws for the size of the gap as a function of E_Z. The size of helical gap will scale linearly, with E_Z in the gate space. The first plateau doesn't scale linearly with E_Z. Further, one can change the parameter θ and sweep V_G back and forth. Helical gap is roughly symmetric while the fake gap has a shard edge. Another characteristic is that size of helical gap goes to zero quicker (non linearly) as $\theta \to \pi/2$ compared to decay of the fake gap as $\theta \to 0$.

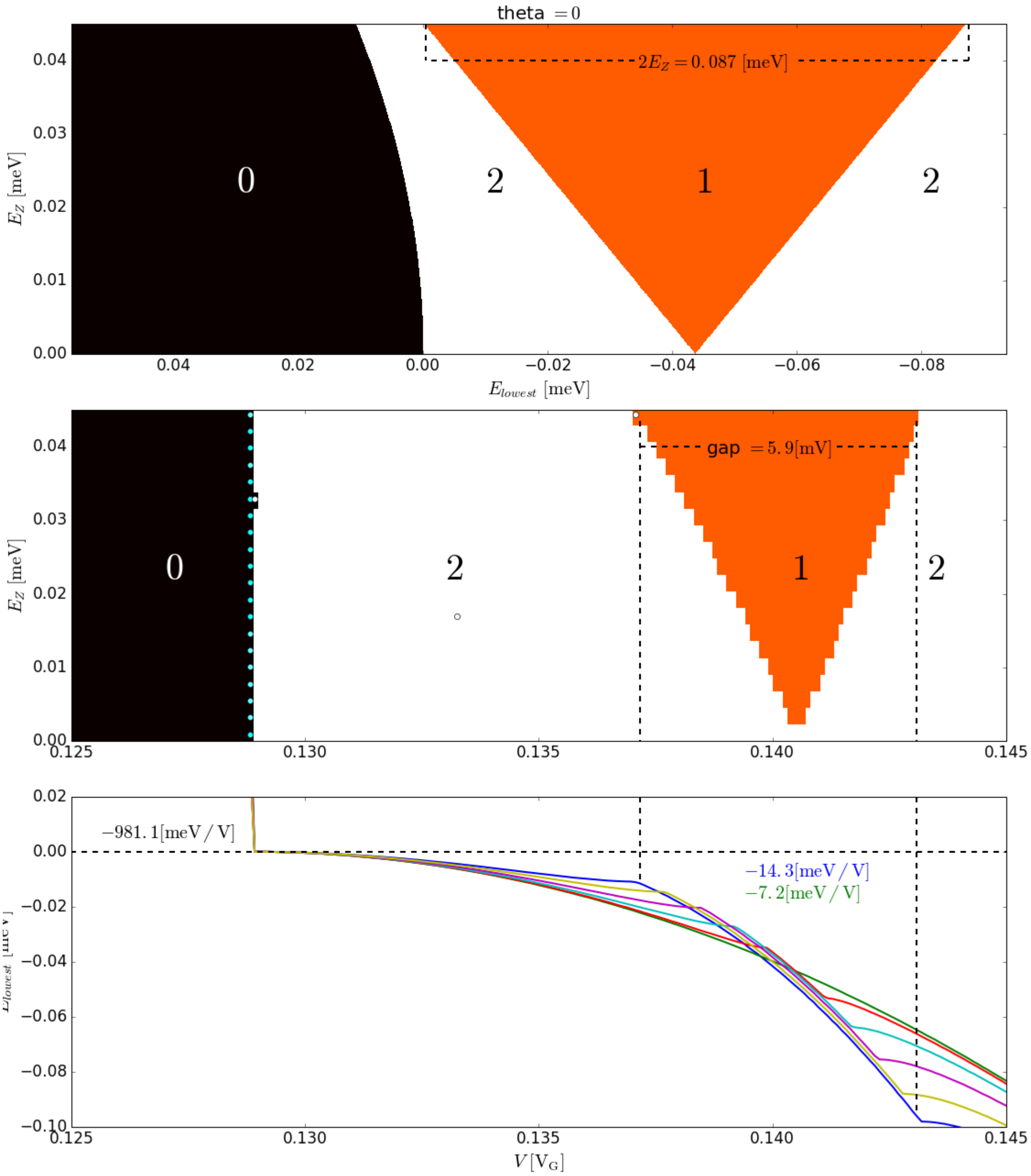

Figure 4.6: Top panel, conductance as a function of the lowest point of dispersion and the Zeeman energy. Middle panel, conductance as a function of V_G and E_Z. Dots represent points where the process of temperature annealing failed, with color relating to final temperature. Lowest panel, plots of the lowest point of energy dispersion as a function of V_G for various values of E_Z. Blue corresponds to the top line of middle plot and green is the case of $E_Z = 0$. l_{SO} is fixed at 250nm for all calculations.

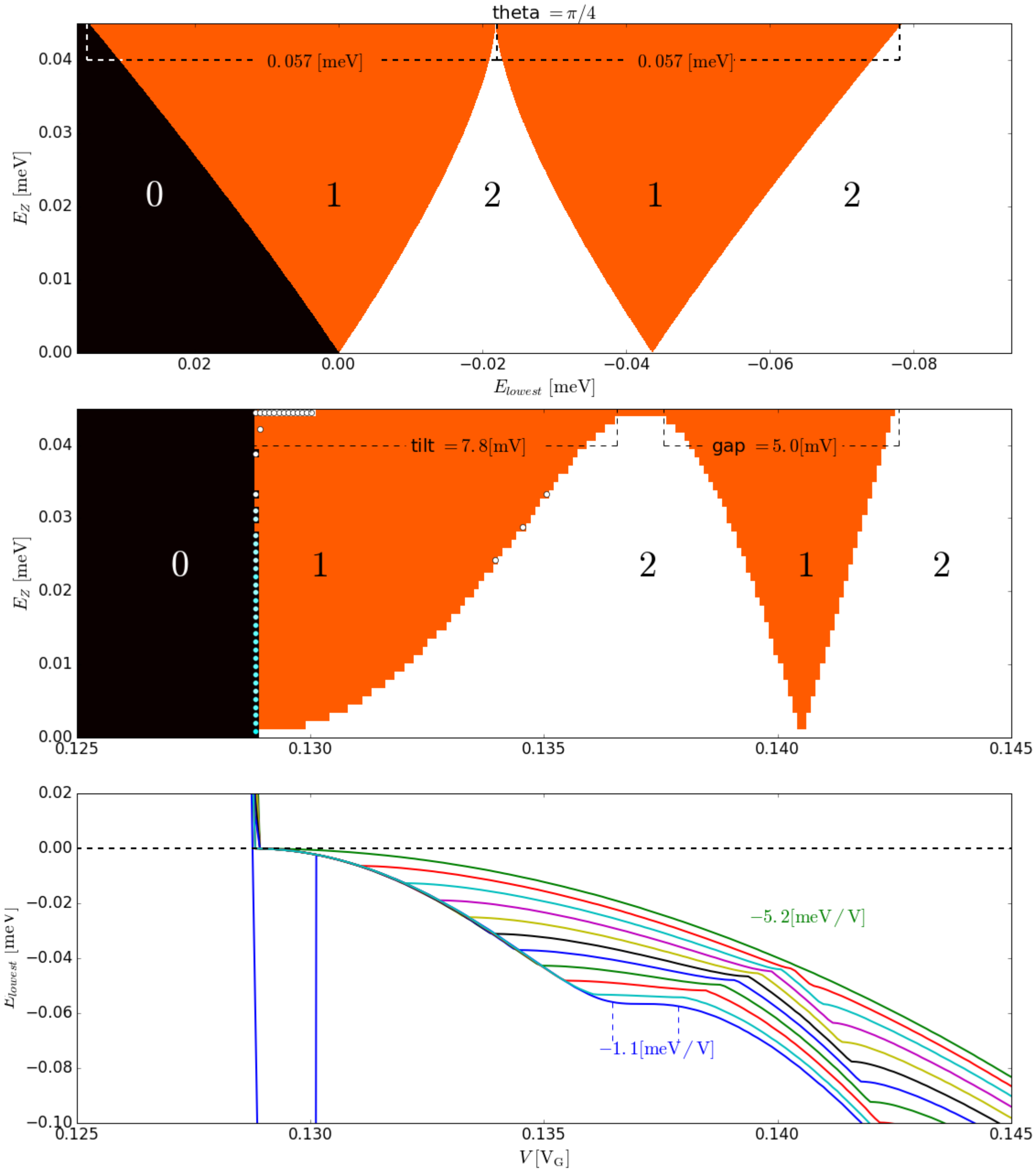

Figure 4.7: Top panel, conductance as a function of the lowest point of dispersion and the Zeeman energy. Middle panel, conductance as a function of V_G and E_Z. Dots represent points where the process of temperature annealing failed, with color relating to final temperature. Lowest panel, plots of the lowest point of energy dispersion as a function of V_G for various values of E_Z. Blue corresponds to the top line of middle plot and green is the case of $E_Z = 0$. l_{SO} is fixed at 250nm for all calculations.

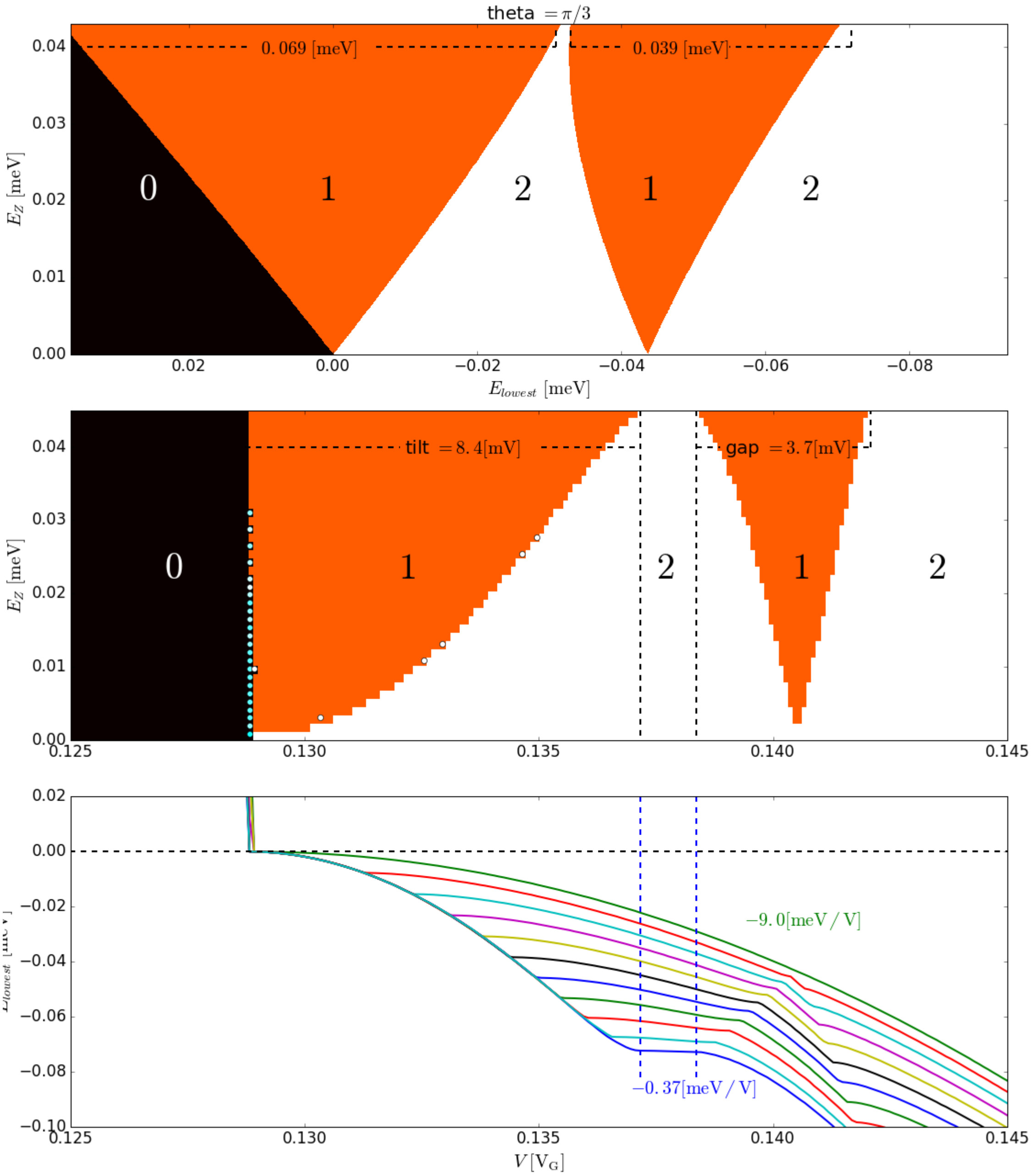

Figure 4.8: Top panel, conductance as a function of the lowest point of dispersion and the Zeeman energy. Middle panel, conductance as a function of V_G and E_Z. Dots represent points where the process of temperature annealing failed, with color relating to final temperature. Lowest panel, plots of the lowest point of energy dispersion as a function of V_G for various values of E_Z. Blue corresponds to the top line of middle plot and green is the case of $E_Z = 0$. l_{SO} is fixed at 250nm for all calculations.

Chapter 5

Conclusion

In this project, nanowire devices have been approximated by a 3D wire, shaped like a hexagon in the x and y direction and infinite in the z axis. The electrostatics due to electrons in the system has been described as a nonlinear coupling of Schrodinger and Poisson equations. These equations have been solved numerically using an algorithm based on the Anderson Mixing Scheme. One can find the algorithm and simulations used on the GitLab.

Anderson solver is a highly robust solver and attempts to improve it by finding the optimal parameters weren't fruit full. The memory and relaxation parameters were sweep for simulations with varying degree of difficulty, yet no useful general trends were derived from it.

The SP solver wasn't able to previously operate on changing direction of magnetic field θ and to solve this problem the algorithm has been extended, and is now able to solve systems for magnetic field in any direction instead of just along the wire. Furthermore a temperature annealing subroutine has been introduced to improve convergence at energies close to van Hove singularities. Whilst this subroutine doesn't guarantee convergence of the solver for zero Kelvin, it does converge in the range of tens mili Kelvin.

Voltage gate dependency of energies has been studied, with focus on conductance. Energies of global backgate devices have an almost degenerate first orbital energy, most likely due to the rotational symmetry of the system. This energy degeneracy is broken for high gate voltages. Scaling properties of the 1 conductance features have been studied. Size of the helical gap proved to scale linearly with Zeeman energy E_Z. Yet, the first conductance of 1 plateau doesn't scale linearly with the E_Z in V_G space and is bigger in the V_G space than the helical gap, even though special energy relations are imposed on the energy dispersion to make both plateaus the same size in the energy domain. The edge of this plateau is sharp instead of smooth egg like shape. In practical applications, where the magnetic field isn't perfectly aligned with the wire, this feature can be mistaken for the helical gap. One can avoid this mistake by sweeping the E_Z looking for linear scaling laws and by sweeping the θ as helical gap closes quicker as $\theta \to \pi/2$ than the 1 conductance plateau as $\theta \to 0$. A theoretical conductance-phase curve has been provided as a function of cross-area energy E_i and tilt in the magnetic field direction θ and has been compared to more realistic approach, describing the system in terms of θ and gate voltage V_G. Analysis of different conduction phases and behaviour of energies in this phase showed the density to remain constant in the helical gap for all values of θ except for $\pi/2$ for which the gap ceases to exist.

Chapter 6

Acknowledgements

I would like thank many people involved in the project, specifically A. Vuik as without him and lots of his time spent on me whenever I interrupted his work, most of the physics involved in this project would remain a mystery to me till this day, R. Skolasinski for lots of technical assistance, especially when I first joined the ranks of Linux users. M. Wimmer for his patient and structured approach to my chaotic work attitude and M. van Gijzen for enforcing proper progress of the project.

The Theoretical Physics group deserves a special acknowledgement. I enjoyed being a part of this community for almost a year immensely and am truly gratefully for the opportunity to experience both the social and professional part of physics research first hand. A. Akhmerov made sure I was an involved member of the research group Quantum Tinkerer from my first days.

Lastly, I would like to thank MathStack Exchange users Andreas and Yuri Negometyanov for a valuable discussion.

Appendix A

Energy dispersion

Write $\mathcal{H} = H_z + H_{x,y}$ as in chapter 2.4

Those two operators, commute with each other and relation

$$H_z\Psi_{i,k} + H_{x,y}\Psi_{i,k} = E\Psi_{i,k} \iff \mathcal{H}\Psi_{i,k} = E\Psi_{i,k} \tag{A.1}$$

holds. The eigenvalue of first operation can be easily found by setting the $\begin{bmatrix} \uparrow \\ \downarrow \end{bmatrix}$ term to a linear combination of spin up and down states of the form $\gamma \begin{bmatrix} 1 \\ 0 \end{bmatrix} + \beta \begin{bmatrix} 0 \\ 1 \end{bmatrix}$. Now, note that wavemode in the cross section does not interact with any of the operators, and the z dependent part retains it's exponential form, one can thus divide it out. Equation left reads:

$$\begin{bmatrix} k^2 + E_Z\cos(\theta) & -i\alpha k - iE_Z\sin(\theta) \\ i\alpha k + iE_Z\sin(\theta) & k^2 - E_Z\cos(\theta) \end{bmatrix} \begin{bmatrix} \gamma \\ \beta \end{bmatrix} = \tilde{E} \begin{bmatrix} \gamma \\ \beta \end{bmatrix} \tag{A.2}$$

With $\tilde{E}$ the eigenenergy of H_z. This, is now again an eigenvalue - eigenvector problem, but now a simpler one as it only regards a 2x2 matrix. One can further derive:

$$\begin{aligned} (k^2 + E_Z\cos(\theta) - \tilde{E})(k^2 - E_Z\cos(\theta) - \tilde{E}) &= (\alpha k + E_Z\sin(\theta))^2 \\ &\iff \\ (k^2 - \tilde{E})^2 &= (\alpha k + E_Z\sin(\theta))^2 + (E_Z\cos(\theta))^2 \\ &\iff \\ \tilde{E} &= k^2 \pm \sqrt{(\alpha k + E_Z\sin(\theta))^2 + (E_Z\cos(\theta))^2} \end{aligned}$$

Now, denote the eigenenergies of $H_{x,y}$ by E_i and using A.1 we conclude:

$$E(k) = k^2 + E_i \pm \sqrt{(\alpha k + E_Z\sin(\theta))^2 + (E_Z\cos(\theta))^2} \tag{A.3}$$

Appendix B

Shape of dispersion

The approach used in this appendix originates from conversations with Math StackExchange [11] users Andreas and Yuri Negometyanov.

Shape of conductance is determined by the shape of energy dispersion (2.19). Also, algorithm doing density of states calculations as described in section 3.1.2. For this reason, one wants to determine the amount of minima and maxima the energy dispersion has. The upper branch of the dispersion, the + case of (2.19), goes to ∞ as $k \to \pm\infty$ and consists only of positive terms. Trivially, it has but one minimum.

Lower branch, corresponding to the $-$ case of (2.19), isn't as simple. It too goes of to infinity for large k but the square root term can be larger than k^2 for some interval forcing the dispersion to have two (by symmetry) minimums and one maxima in between. Consider the derivative of $E(k)$ for α,$E_Z \neq 0$:

$$E'(k) = 2k - \frac{\alpha(\alpha k + E_Z \sin(\theta))}{\sqrt{(\alpha k + E_Z \sin(\theta))^2 + E_Z^2 \cos^2(\theta)}}. \tag{B.1}$$

We set the equation equal zero, and work out:

$$E'(k) = 0 \tag{B.2}$$

$$2k = \frac{\alpha(\alpha k + E_Z \sin(\theta))}{\sqrt{(\alpha k + E_Z \sin(\theta))^2 + E_Z^2 \cos^2(\theta)}} \tag{B.3}$$

$$4k^2\big((\alpha k + E_Z \sin(\theta))^2 + E_Z^2 \cos^2(\theta)\big) = \alpha^2\big(\alpha k + E_Z \sin(\theta)\big)^2 \tag{B.4}$$

Note that because of the squaring of both sides, we generate more solutions corresponding to the case:

$$2k = -\frac{\alpha(\alpha k + E_Z \sin(\theta))}{\sqrt{(\alpha k + E_Z \sin(\theta))^2 + E_Z^2 \cos^2(\theta)}}, \tag{B.5}$$

to account for this we must thus require $\mathrm{sign}(k) = \mathrm{sign}\big(\alpha k + E_Z \sin(\theta)\big)$.

Equation (B.4) can be simplified by a linear transformation to a variable x defined as $k = \frac{E_Z}{\alpha}\big(x - \sin(\theta)\big)$. Linear transformations re-size and translate the space they work on, so they don't change the existence of topological features like minimums and maximums. In terms of the new variable the equation reads:

$$4\left(\frac{E_Z}{\alpha}\right)^2 \big(x-\sin(\theta)\big)^2 \big(E_Z^2x^2 + E_Z^2\cos^2(\theta)\big) = \alpha^2 E_Z^2 x^2 \tag{B.6}$$

$$4E_Z^4\big(x-\sin(\theta)\big)^2 \big(x^2 + \cos^2(\theta)\big) = \alpha^4 E_Z^2 x^2 \tag{B.7}$$

$$\big(x-\sin(\theta)\big)^2 \big(x^2 + \cos^2(\theta)\big) = \frac{\alpha^4}{4E_Z^2} x^2 \tag{B.8}$$

The quantity $\frac{\alpha^4}{4E_Z^2}$,instead of α or E_Z on it's own, determines the amount of solution and hence we will denote it by λ. For $\theta = n\pi$ with $n \in \mathcal{Z}$ the equations simply read $x^2(x^2+1) = \lambda x^2$. $x = 0$ is trivially a solution to the equation. For other solution can be obtained by dividing the x^2 factor out, and reads $x = \pm\sqrt{\lambda - 1}$. Since, for $\theta = 0$ we automatically meet the requirement of correct signs and thus for $\lambda > 1$ the bottom band has 3 local maximums or minimums, and thus 2 minima's and one maximums ($E(k) \to \infty$ as $|k| \to \infty$) and one minimums otherwise. This is the same as requiring $\alpha^2 > 2E_Z$ for W-shaped dispersion.

For $\theta \neq n\pi$ one can define yet another linear transformation $x = z\sin(\theta)$. Note that a linear transformation of a linear transformation is, in itself a linear transformation so the existence of minimums and maximums in conserved. One can further simplify equations:

$$\big(z\sin(\theta) - \sin(\theta)\big)^2 \big(z^2\sin^2(\theta) + \cos^2(\theta)\big) = \lambda z^2 \sin^2(\theta) \tag{B.9}$$

$$\sin^2(\theta)(z-1)^2 \big(z^2\sin^2(\theta) + \cos^2(\theta)\big) = \lambda z^2 \sin^2(\theta) \tag{B.10}$$

$$\big(z^2\sin^2(\theta) + \cos^2(\theta)\big) = \lambda \frac{z^2}{(z-1)^2} \tag{B.11}$$

Number of solutions for equation (B.11) coincides with the number of energy dispersion $E(k)$. RHS is singular for $z = 1$. Yet observe, that sing restriction reads:

$$\begin{aligned}
&\operatorname{sign}(k) = \operatorname{sign}\big(\alpha k + E_Z \sin(\theta)\big)\\
&\operatorname{sign}\big(x - \sin(\theta)\big) = \operatorname{sign}(x) \text{ since } E_Z > 0 \text{ and } \alpha > 0\\
&\operatorname{sign}\big(z\sin(\theta) - \sin(\theta)\big) = \operatorname{sign}(z\sin(\theta))\\
&\operatorname{sign}(z-1) = \operatorname{sign}(z) \Rightarrow z \notin (0,1).
\end{aligned}$$

Thus, the valid solutions have either $z < 0$ or $z > 1$. Observe for the LHS that at $z = 0$ equals $\cos^2(\theta) \geq 0$ and for $z \to \infty$ it diverges. On the other hand RHS is zero for $z = 0$ and monotonic decreasing function for $z > 1$ with limit of λ as $z \to \infty$. Thus equation (B.11) has one solution for $z > 1$.

Lets now consider the $z < 0$ case. RHS has a limit of λ as well, but it reaches the limit monotonically from below as opposed to reaching it from above compared to the other case. LHS experiences the same behaviour as in the last case. Thus, for fixed θ the value of λ determines amount of intersections. For a small λ one expects no intersections, big λ exactly two and somewhere in between LHS and RHS will touch but not intersect. This will result in a saddle point in the energy dispersion. In order to calculate the value of λ for which one obtains a saddle point, LHS and RHS needs to have both the same function values and derivatives. Calculating the point where this happens goes as:

$$2z\sin^2(\theta) = -2\lambda\frac{z}{(z-1)^3} \tag{B.12}$$

$$(z-1)^3 = -\frac{\lambda}{\sin^2(\theta)} \tag{B.13}$$

$$z = 1 - \sqrt[3]{\left(\frac{\lambda}{\sin^2(\theta)}\right)}. \tag{B.14}$$

Finally, plugging the z into the expressions from equation (B.11) gives:

$$\left(1 - \sqrt[3]{\left(\frac{\lambda}{\sin^2(\theta)}\right)}\right)^2 \sin^2(\theta) + \cos^2(\theta) = \lambda\left(1 - \sqrt[3]{\left(\frac{\lambda}{\sin^2(\theta)}\right)}\right)^2 \left(\sqrt[3]{\left(\frac{\lambda}{\sin^2(\theta)}\right)}\right)^{-2}$$

This equation simplifies to the relation:

$$\lambda = \left(\cos^{2/3}(\theta) + \sin^{2/3}(\theta)\right)^3, \tag{B.15}$$

one can now observe three important facts. First, case $\theta = 0$ reads $\lambda = 1$ a result we already have obtained. Secondly RHS of equation (B.15) has a maximum of 4 for $\theta = \pi/4$. Thus, if $\lambda > 4$ the energy dispersion will have a W shape for all values of θ. Finally for $1 \leq \lambda \leq 4$ the energy dispersion will go from having 3 extrema to only 1 for some θ range centered around $\pi/4$.

Appendix C

Conduction edge

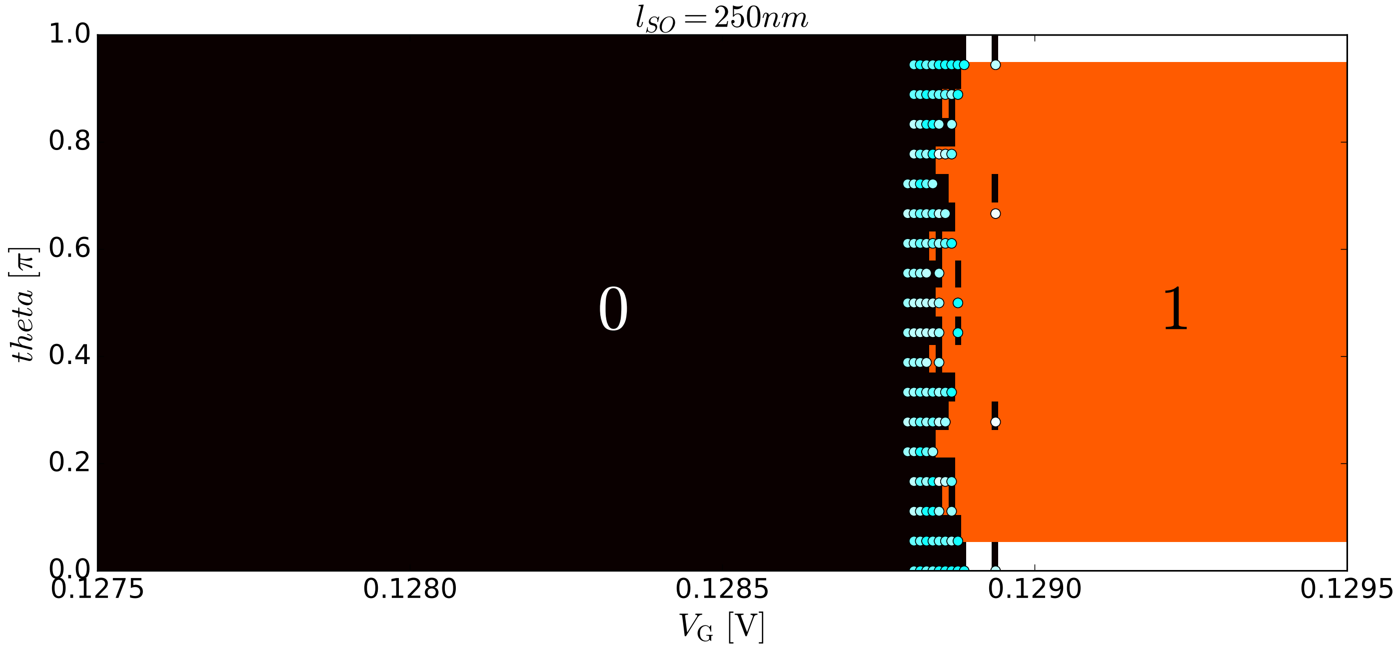

Figure C.1: Zoom in on the sharp edge of the $0 \rightarrow 1$ conductance transition. The resolution in θ is 4 times lower in this plot as compared to figure 4.5. One can still observe the edge to lose it's sharpness as expected. This transition is the hardest for the Anderson solver, as mentioned in chapter 4.2, so one see's many points for which the solver failed to converge, denoted by the blue dots. Typical temperature for which the convergence failed is about 60 mK. The voltage gate spacing used in this plot is 10^{-5}V and yet the non sharp edge of the gap is barely to be seen. One can safely assume that for all practical purposed the band edge is sharp.

Bibliography

[1] Kittel, Charles (1996). *Introduction to Solid State Physics.* New York: Wiley. ISBN 0-471-14286-7

[2] A. Vuik, *Effects of the electrostatic environment on the Majorana nanowire devices*, Master Thesis

[3] A. Vuik, D. Eeltink, A. R. Akhmerov, M. Wimmer *Effects of the electrostatic environment on the Majorana nanowire devices*, New J. Phys. 3, 033013 (2016), [arXiv:1511.08044]

[4] A. Manchon, H.C. Koo, J. Nitta, S.M. Frolov, R.A. Duine *New Perspectives for Rashba Spin-Orbit Coupling* Nature Materials 14, 871–882 (2015), [arXiv:1507.02408] [10.1038/nmat4360]

[5] Peng Ni, *Anderson Acceleration of Fixed-point Iteration with Applications to Electronic Structure Computations*

[6] V. Eyert, *A Comparative Study on Methods for Convergence Acceleration of Iterative Vector Sequences*, J. Comp. Phys. Volume 124, Issue 2, 15 March 1996, Pages 271-285 [doi:10.1006/jcph.1996.0059]

[7] Press, W. H.; Flannery, B. P.; Teukolsky, S. A.; and Vetterling, W. T. *Numerical Recipes in FORTRAN: The Art of Scientific Computing, 2nd ed. Cambridge, England: Cambridge University Press*, 1988, Pages 352 - 355

[8] Léon Van Hove, *The Occurrence of Singularities in the Elastic Frequency Distribution of a Crystal*, Phys. Rev. 89, 1189

[9] C. W. Groth, M. Wimmer, A. R. Akhmerov, X. Waintal, *Kwant: a software package for quantum transport*, New J. Phys. 16, 063065 (2014)

[10] A. Logg and G. N. Wells (2010). *DOLFIN: Automated Finite Element Computing, ACM Transactions on Mathematical Software, 37(2).* [doi:10.1145/1731022.1731030] [arXiv:1103.6248]

[11] http://math.stackexchange.com/questions/1897138/maxima-of-almost-quadratic-function